SANDIA REPORT
SAND2017-11157
Unlimited Release
Printed October 2017

Hydrogen Fuel Cell Electric Vehicle Tunnel Safety Study

Chris LaFleur, Gabriela Bran-Anleu, Alice B. Muna, Brian D. Ehrhart, Myra Blaylock, William G. Houf

Prepared by
Sandia National Laboratories
Albuquerque, New Mexico 87185 and Livermore, California 94550

Sandia National Laboratories is a multimission laboratory managed and operated by National Technology and Engineering Solutions of Sandia, LLC, a wholly owned subsidiary of Honeywell International, Inc., for the U.S. Department of Energy's National Nuclear Security Administration under contract DE-NA0003525.

Sandia National Laboratories

Issued by Sandia National Laboratories, operated for the United States Department of Energy by National Technology and Engineering Solutions of Sandia, LLC.

Printed in the United States of America. This report has been reproduced directly from the best available copy.

Available to DOE and DOE contractors from
U.S. Department of Energy
Office of Scientific and Technical Information
P.O. Box 62
Oak Ridge, TN 37831

Telephone: (865) 576-8401
Facsimile: (865) 576-5728
E-Mail: reports@osti.gov
Online ordering: http://www.osti.gov/scitech

Available to the public from
U.S. Department of Commerce
National Technical Information Service
5301 Shawnee Rd
Alexandria, VA 22312

Telephone: (800) 553-6847
Facsimile: (703) 605-6900
E-Mail: orders@ntis.gov
Online order: http://www.ntis.gov/search

SAND2017-11157
October 2017
Unlimited Release

Hydrogen Fuel Cell Electric Vehicle Tunnel Safety Study

Chris LaFleur, Alice B. Muna, Brian D. Ehrhart
Risk and Reliability Analysis
Sandia National Laboratories
P. O. Box 5800
Albuquerque, New Mexico 87185-0748

Gabriela Bran-Anleu, Myra Blaylock
Thermal/Fluid Science and Engineering
Sandia National Laboratories
P. O. Box 969
Livermore, California 94551-0969

William G. Houf
Consultant to Sandia National Laboratories, Livermore

Abstract

Several jurisdictions with critical tunnel infrastructure have expressed the need to understand the risks and implications of traffic incidents in tunnels involving hydrogen fuel cell vehicles. A risk analysis was performed to estimate what scenarios were most likely to occur in the event of a crash. The results show that the most likely consequence is no additional hazard from the hydrogen, although some factors need additional data and study to validate. This includes minor crashes and scenarios with no release or ignition. When the hydrogen does ignite, it is most likely a jet flame from the pressure relief device release due to a hydrocarbon fire. This scenario was considered in detailed modeling of specific tunnel configurations, as well as discussion of consequence concerns from the Massachusetts Department of Transportation. Localized concrete spalling may result where the jet flame impinges the ceiling, but this is not expected to occur with ventilation. Structural epoxy remains well below the degradation temperature. The total stress on the steel structure was significantly lower than the yield stress of stainless and ASTM A36 steel at the maximum steel temperature even when the ventilation was not operational. As a result, the steel structure will not be compromised. It is important to note that the study took a conservative approach in several factors, so observed temperatures should be lower than predicted by the models.

ACKNOWLEDGMENTS

This work was supported by the U. S. Department of Energy, Office of Energy Efficiency and Renewable Energy, Hydrogen, Fuel Cells and Infrastructure Technologies Program. The authors wish to thank Paul LaFleur of the Federal Highway Safety Administration for his help in identifying vehicle crash data. The authors also wish to thank Joe Rigney of the Massachusetts Department of Transportation for his help in providing tunnel information and feedback on the analysis. Finally, the authors with to thank Will James and Laura Hill of FCTO for their leadership in this analysis, as well as Jay Keller (consultant), Nick Barilo (PNNL), and Carl Rivkin (NREL) who provided very useful feedback on the analysis and report.

CONTENTS

FIGURES

TABLES

NOMENCLATURE

Abbreviation	Definition
AHJ	Authority having jurisdiction
CANA	Central Artery North Area
CFD	Computational fluid dynamics
CNG	Compressed natural gas
CVFEM	Control volume finite element model
DOT	Department of Transportation
EDC	Eddy dissipation concept
ESD	Event sequence diagram
FCEV	Fuel cell electric vehicle
FCTO	Fuel Cell Technologies Office
FEM	Finite element method
FMVSS	Federal Motor Vehicle Safety Standards
GTR	Global Technical Regulation
HC	Hydrocarbon
HGV	Heavy goods vehicle
HRR	Heat release rate
ISO	International Organization for Standardization
MUSCL	Monotonic upwind scheme for conservation laws
NFPA	National Fire Protection Association
NHTSA	National Highway Traffic Safety Administration
NREL	National Renewable Energy Laboratory
OEM	Original equipment manufacturer
PDE	Partial differential equation
PE	Polyethylene
PMR	Participating media radiation
PNNL	Pacific Northwest National Laboratory
PS	Polystyrene
PUR	Polyurethane
RANS	Reynolds-averaged Navier-Stokes
RWS	Rijkswaterstaat, a time-temperature curve used in safety standards
SNL	Sandia National Laboratories
SUV	Sport utility vehicle

Abbreviation	Definition
TNO	Netherlands Organization for Applied Scientific Research
TPRD	Thermally-activated pressure relief device

1. INTRODUCTION

As the technology and infrastructure for hydrogen fuel cell electric vehicles (FCEV) develops, they will become more prevalent on public roads and highways worldwide. In the United States FCEVs and the required infrastructure to support them has been initiated in the state of California. The next region that will see the introduction of FCEVs is the northeast corridor, a region stretching from Washington DC to Boston. As the geographical extent of FCEVs increases, the impact of these vehicles on different road structures must be considered. The focus of these analyses is on tunnels. Several jurisdictions that have tunnels that serve as significant transportation arteries in major metropolitan areas have expressed the need to understand the risks and implications of traffic incidents in tunnels involving FCEVs. As a result, the DOE's Fuel Cell Technologies Office (FCTO), under the Office of Energy Efficiency and Renewable Energy, convened a team of hydrogen and risk experts from Sandia National Laboratories (SNL), Pacific Northwest National Laboratory (PNNL), National Renewable Energy Laboratory (NREL) as well as FCTO staff and consultants to provide scientific analysis and characterizations of the hydrogen behavior to allow the authorities to make informed decisions about permitting FCEVs in their tunnels. The team also provided information and resources for emergency responders that would be called upon to respond to traffic incidents involving FCEVs, but it is not within the scope of this report.

This report provides key information on the requirements that FCEVs and their hydrogen storage systems must meet. It also documents the comprehensive risk framework, analysis, and quantification for potential traffic incidents in tunnels. The results of the risk analysis indicated that detailed modeling and simulation was needed to characterize a specific scenario involving a hydrogen jet flame from a pressure relief valve. The results of the modeling are included as well as discussion of specific consequence concerns communicated by the Massachusetts Department of Transportation.

2. HYDROGEN VEHICLE AND TUNNEL SAFETY REQUIREMENTS

Hydrogen vehicles have robust requirements which evolved from other alternative fuel vehicle requirements, such as compressed natural gas (CNG) as well as from hydrogen release behavior research and experimental studies. This section describes specific requirements pertinent to the protection of the pressure vessel.

2.1. Hydrogen Pressure Vessel Requirements

Hydrogen vehicle fuel is contained in a composite overwrapped pressure vessel and stored in the gaseous state. The pressure vessel includes a thermal pressure relief device (TPRD) which, in the event of a fire, releases the hydrogen to prevent the vessel from over-pressurizing. Current storage systems have pressures of up to 10,000 psi (70 MPa). Global Technical Regulation No. 13 (GTR #13) [1] provides requirements for the integrity of compressed and liquid hydrogen motor vehicle fuel systems. The test procedures and methods specified in GTR #13 include pressure cycling tests (pneumatic and hydraulic with temperature variations), a burst test, a permeation test, and a bonfire test (localized and engulfing). The pressure cycling test evaluates a container's durability to withstand, without burst, 22,000 cycles of pressurization and depressurization. The burst test evaluates a container's initial strength and resistance to degradation over time. The bonfire test evaluates the ability of the container's TPRD to open in a fire scenario. This test starts with a localized fire at 600°C impinging on a portion of the tank distant from the TPRD for 10 min, followed by an engulfing fire at 800°C for an additional 10 minutes. The TPRD must release before the end of the test and this release must be uninterrupted until the tank reaches of a pressure of 1 MPa. The tank cannot burst or leak during the test. If the TPRD does not release during test, the tank is considered to have failed. These test requirements are more stringent than the Federal Motor Vehicle Safety Standards (FMVSS) No. 304 requirements for CNG tanks [1].

2.2. Hydrogen Vehicle Requirements

In the U.S., FCEVs are required to undergo the same crash tests as gasoline vehicles. GTR #13 pertains to hydrogen fuel cell vehicles, and the first phase (Phase I) was published in 2013. The intent of the GTR #13 is to establish a global regulation for FCEVs that attains equivalent levels of safety to those for conventional gasoline powered vehicles. The development of Phase I of the GTR involved analyzing hydrogen-powered vehicles based on component and subsystem levels and included learnings from CNG-fueled vehicles. The resulting regulation is more stringent than FMVSS 304 for CNG. For crash testing, the GTR specifies that each participating country will use its existing national crash tests but develop and agree on maximum allowable levels of hydrogen leakage. In the U.S., these national crash tests are found in the FMVSS which includes specified tests for barrier impacts, rear collisions, and side impact crashes. Phase II will involve international harmonization of crash test requirements for FCEV regarding whole vehicle crash testing for fuel system integrity with the intent of creating global standards. The U.S. is adopting the entire GTR #13 requirements with the exception of one related to the electrical resistance of the coolant used for maintaining the temperature of the fuel cell stack into the U.S. Department of Transportation (DOT) family of FMVSS.

2.3. Tunnel Safety Requirements

The National Fire Protection Association Standard 502 (NFPA 502), *Standard for Road Tunnels, Bridges, and Other Limited Access Highways*, provides fire protection and life safety requirements as well as design criteria for authorities having jurisdiction (AHJs) to use in ensuring tunnel safety [2]. In some cases, tunnels may have been constructed before NFPA 502 was written or adopted. In this case, the tunnels meet the construction and ventilation requirements in place at the time they were built. Annex G provides specific recommendations for addressing alternate fuel vehicles and specifically states that in the long term, regulators should be able to rely on the approved listing and labeling to permit these vehicles in road tunnels. Unlike other alternative fueled vehicles, FCEVs are built only by original equipment manufacturers (OEMs) and are required to comply with the same rigorous safety standards as all gasoline- and diesel-fueled vehicles: FMVSS and the GTR.

NFPA 502 Section 7.3.2 states that a structure (road tunnel) shall be capable of withstanding the temperature exposure represented by the Rijkswaterstaat (RWS) time-temperature curve or other recognized standard time-temperature curve that is acceptable to the AHJ, as shown by an engineering analysis. The standard time-temperature curves all describe the gas temperature at the interface with tunnel structures as a function of time for the entire tunnel length. The assumption is that every part of the tunnel should withstand these temperature exposures, irrespective of the fire location, ventilation rate or type. In reality, the construction is not exposed to these time temperature curves over the entire tunnel length and is instead exposed to heat fluxes that are dependent upon the origin of fire, the ventilation rate, the type and amount of fuel (heat release rate), and the size of the cross-section [3]. Descriptions of standard time-temperature fire curves are given below.

2.3.1. The Rijkswaterstaat (RWS) and Other Time-Temperature Curves

Standard fire curves have been used to design for road tunnel safety. This process typically involves selecting an expected type and size of fire and determining the distribution of temperature exposure to the construction materials. For example, the International Organization for Standardization (ISO) 834 curve represents a fully developed fire in a compartment, based on materials found in standard buildings. The ISO curve is what the World Road Association (PIARC) and the International Tunneling Association recommend for defining tunnel design criteria for personal vehicles and vans [4].

Because the ISO 834 curve does not represent all materials, especially chemicals which escalate fire growth, a hydrocarbon curve was developed in the 1970s for use in the petrochemical and off-shore industries and began to be applied to tunnels [5]. The hydrocarbon curve (HC curve) exhibits a faster fire development and consequently is associated with faster temperature increase than the standard ISO 834 curve.

The Rijkswaterstaat (RWS) curve was developed during extensive testing conducted by the Dutch Ministry of Transport in cooperation with the Netherlands Organization for Applied Scientific Research (TNO) in the late 1970s. The RWS curve simulates an accident involving a gasoline tanker loaded with 45,000 liters (45 m^3) of gasoline with a fire load of approximately 300 MW released over two hours [6]. The ISO 834, hydrocarbon, and RWS fire curves are illustrated in

Figure 1. Also included in Figure 1 are the ASTM E119, *Standard Test Method for Fire Test of Building Construction and Materials*, and the UL 1709, *Standard for Rapid Rise Fire Tests of Protection Materials for Structural Steel,* time-temperature fire curves [7, 8].

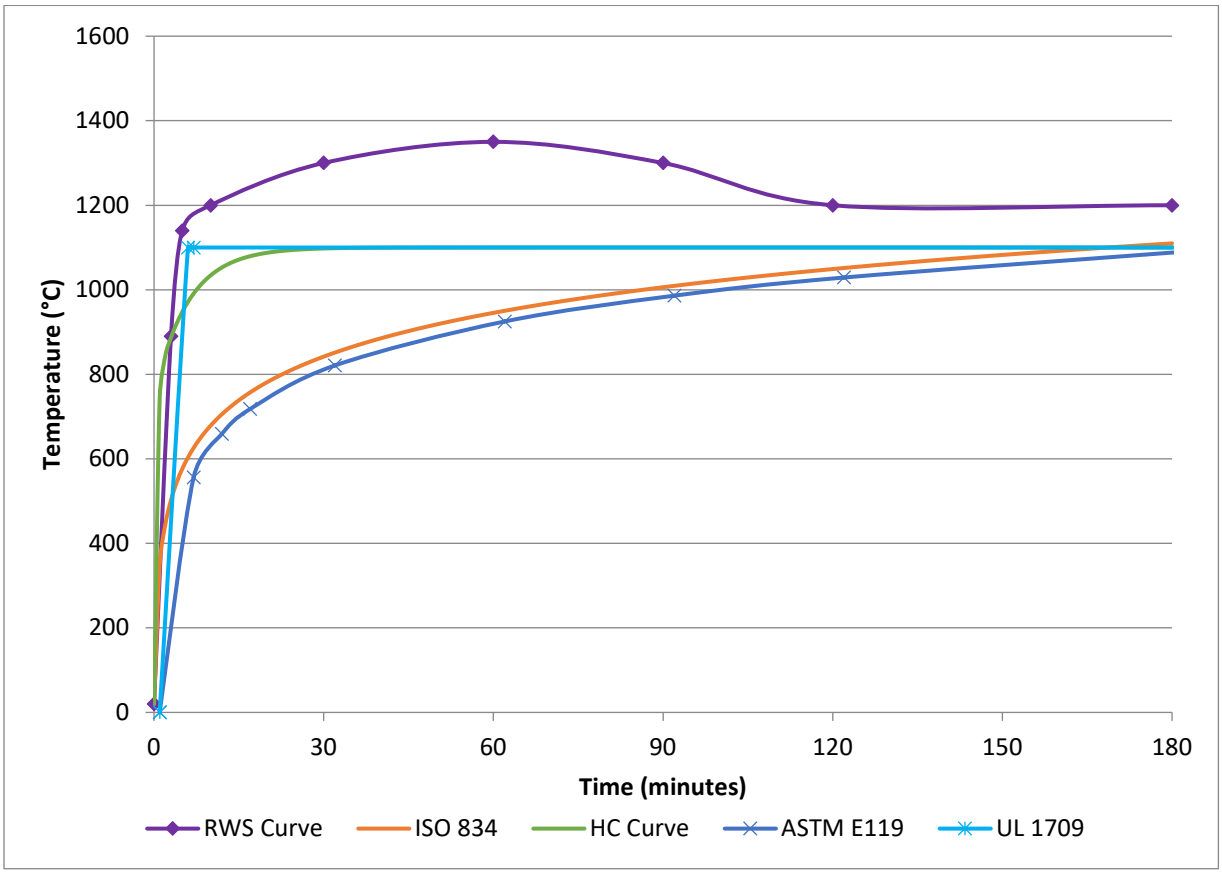

Figure 1: Standard time-temperature fire curves at tunnel structure interfaces for designing tunnels.

2.3.2. The Runehamar Full Scale Tests

In September 2003, a European research program on tunnel safety conducted comprehensive large-scale fire tests in the abandoned Runehamar tunnel road tunnel in Norway [5, 9]. These fire tests were intended to analyze fires in the cargo of heavy goods vehicle (HGV) trailers, which contain a large amount of fuel for a fire. The fuel load of HGV and traditional vehicles is comprised of hydrocarbons and hydrocarbon-based materials (i.e. tires) which form very sooty fires where radiation is the over-riding method of heat transfer to the surrounding materials. The Runehamar tunnel is approximately 1,600 m long, 6 m high, and 9 m wide. The center of the fire was located 172 m from one entrance. Two mobile fan units were added to simulate ventilation, providing a velocity of about 3 m/s (centerline) in the tunnel. Because of the exposure to high temperatures, the tunnel was protected using PROMATECT –T fire protection boards over 75 m that were supported with a light steel structure. Fire sprinklers were not installed in the tunnel. Two small ignition sources, consisting of fiberboard cubes soaked with heptane, were placed within the lowest wood pallets. A total of four tests were performed with a fire in a semi-trailer set-up. In the trailer, four different commodities were tested, shown in Table 1.

Table 1: Commodities used as fuel in the HGV tests.

Test Number	Description of the fire load	Target	Peak Heat Release Rate (HRR) [MW]
1	3600 wood pallets (1,200 x 800 x 150 mm) 20 wood pallets (1,200 x 1000 x 150 mm) 74 polyethylene (PE) plastic pallets (12,200 x 800 x 150 mm)	32 wood pallets and 6 PE pallets	200
2	216 wood pallets 240 polyurethane (PUR) mattresses (1,200 x 800 x 150 mm)	20 wood pallets and 20 PUR mattresses	160
3	Furniture and fixtures (tightly packed plastic and wood cabinet doors, household items) 10 large rubber tires (800 kg)	Upholstered sofa and arm rest	135
4	600 corrugated paper cartons with interiors (600 mm x 400 mm x 500 mm) 15% of total mass of unexpanded polystyrene (PS) cups (18,000 cups) and 40 wood pallets	4 wood pallets and 40 cartons with PS cups (1,800 cups)	65

Test 1 with wood pallets and plastic pallets had the highest heat release rate, with a peak heat release rate of 200 MW. Heat release rate (HRR) is the most important variable in characterizing the 'flammability' of products and their consequent fire hazard because it captures the driving force for the fire (i.e. power) and most other variables (temperature, smoke, toxic gases) are correlated to heat release rate [10]. Further, the maximum excess gas temperatures beneath the ceiling were approximately 1,350°C. Figure 2 illustrates the heat release rates for the four large-scale tests. Figure 3 illustrates gas temperatures in the first test, which had the highest temperatures out of the four tests, compared with four different standard fire curves. All tests produced time-temperature developments in line with the RWS curve, as stated in NFPA 502.

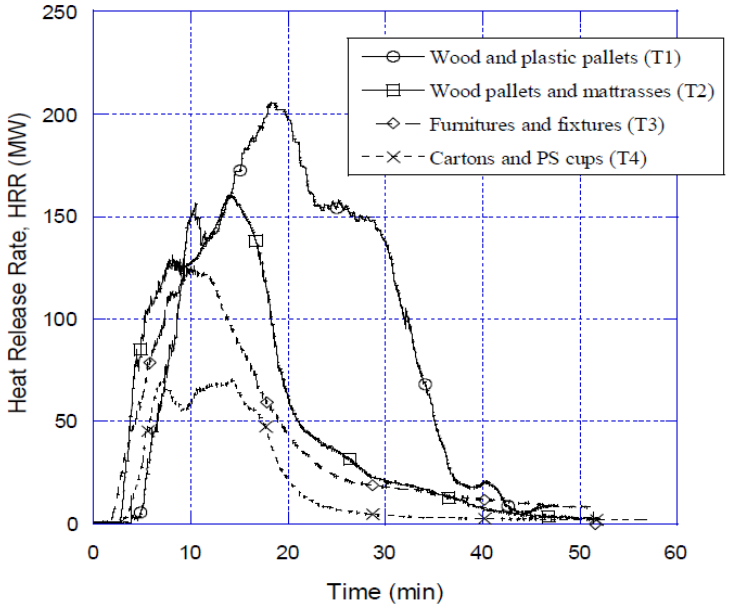

Figure 2: Heat release rates from the four large-scale fire tests.

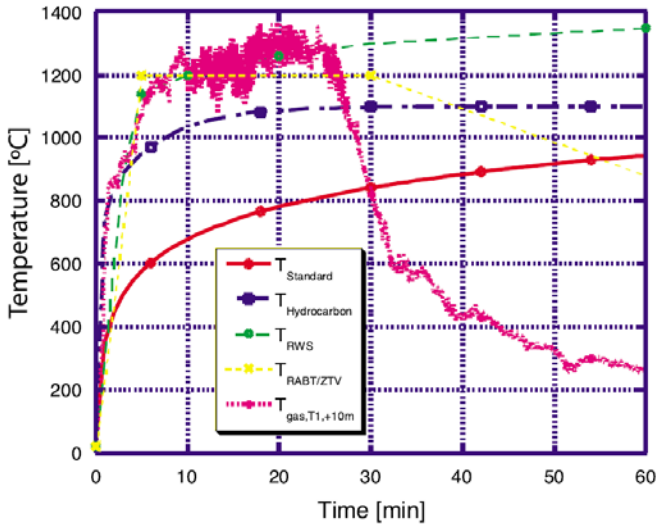

Figure 3: Gas temperatures at tunnel structure interface in test 1 compared with standard fire curves.

The results from the Runehamar tunnel tests show that non-hazardous, solid commodities can give a fast increase in temperatures to significantly higher temperatures than had been measured in connection with solid material in tunnel fire tests previously [5]. The temperatures measured in the post-flame gases downstream of the fire were high and the measurements indicate that the flaming zone could expand up to a length of 70-100 m. The high surface temperatures affected the entire tunnel ceiling downstream of the fire causing considerable spalling of the unprotected tunnel ceiling after the first test, which resulted in considerable rock debris completely covering the road. The long flames and high temperatures could also cause the fire to spread to other vehicles.

The intent of NFPA 502 is to establish minimum criteria that provide protection from fire for road tunnels. However, not all existing tunnels meet all NFPA 502 requirements because they were built prior to this requirement or may have not been subject to this standard.

Section G.3 of NFPA 502 provides guidance for hazard mitigation measures such as ventilation, reduction of ceiling pockets, installation of detectors in high points, labeling of alternate fuel vehicles, and emergency responder training and equipment. NFPA 502 also states that the AHJ is "responsible for evaluating each tunnel on a case-by-case basis … by risk analysis, computer modeling, experimental testing or all of the above." Although the safety standards and regulations for FCEVs are more developed than when that guidance was written in NFPA 502, a risk analysis may still be warranted.

3. RISK ANALYSIS

A framework for risk analysis consists of identifying what can happen, how likely it is to happen, and what the consequences are if it does happen. This tool was selected to provide a logical, visual framework to catalogue the different potential outcomes of various magnitude incidents in road tunnels. This section provides a detailed construction and explanation of an event tree used to analyze the risks of FCEVs in tunnels. An overview of a previous alternate fueled vehicle risk study performed for tunnels is included in Appendix A to provide a historical reference to similar research performed for tunnels in the U.S.

3.1. Event Sequence Diagram

An event sequence diagram (ESD) is a tool used in risk assessments to represent an undesired event as a sequence of sub-events [11]. An event tree presents a visual representation of all possible scenarios and is particularly useful for calculating how multiple safeguards can affect the consequence. The event tree begins with an initiating event and illustrates the chronological sequence of events involving the successes and/or failures of the system components. Each bifurcation is assigned a probability of occurrence and thus the probability of various possible outcomes can be calculated. The total for each outcome is the summation of all the probabilities leading to that outcome. The paths are chronological, left to right, and show the events as they occur in time. All outcomes along with the values and probabilities associated with them are shown on the tree. An event sequence diagram for a hydrogen vehicle accident is illustrated in Figure 4 and will be discussed in detail throughout this chapter.

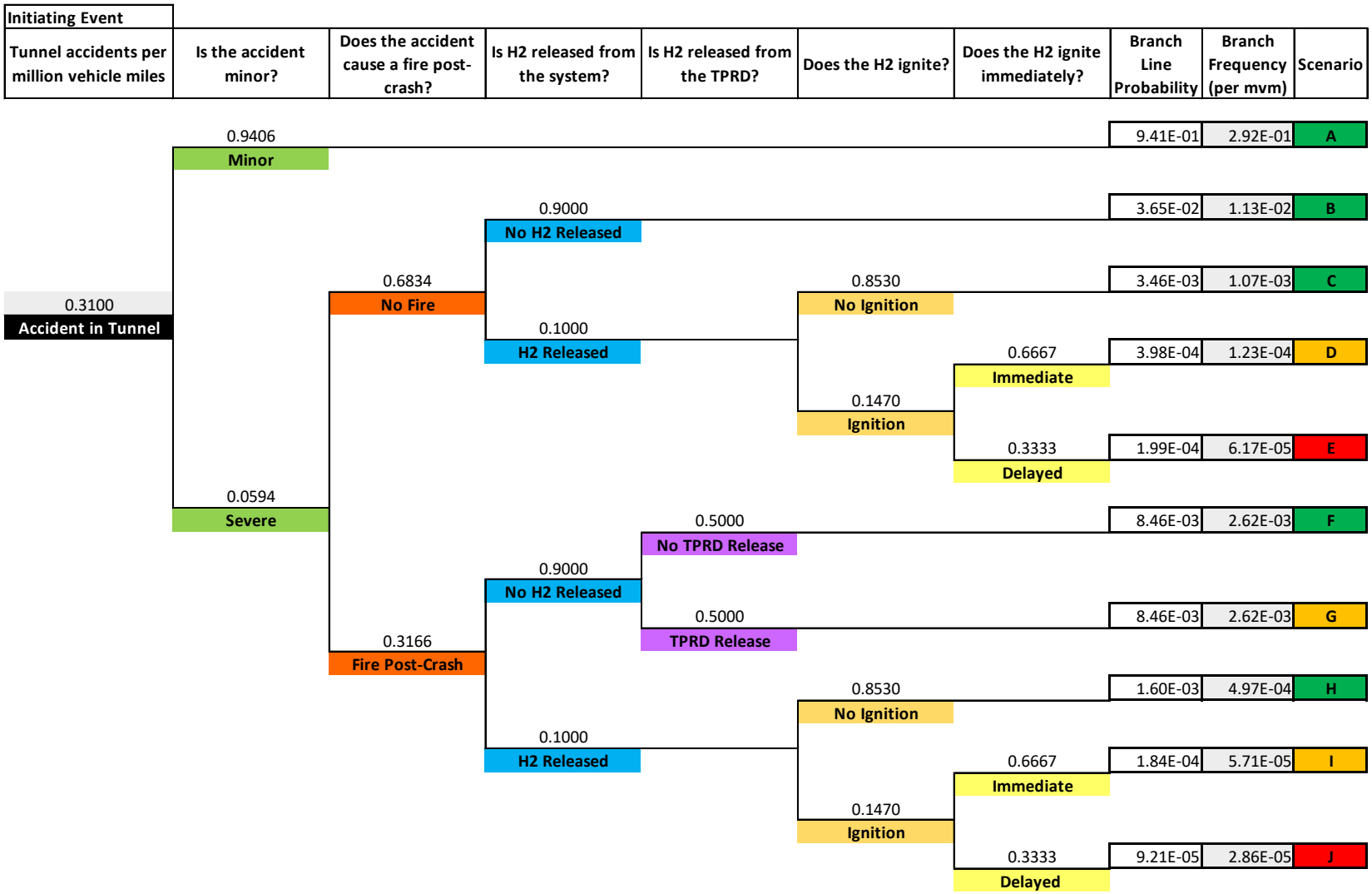

Figure 4: Event sequence diagram for a hydrogen vehicle accident.

3.1.1. Hydrogen Vehicle Accident in Tunnel Event

The initiating event for the event tree is an accident involving a FCEV in a tunnel. Since there are currently no published data sources for FCEV accidents in tunnels specifically, this analysis uses the generic accident rate for tunnels conservatively. Over time, the number of FCEVs on the road will increase so it is expected that this proportion will change with time. Where possible, every attempt was made to use U.S. data in calculating the success and failure probabilities in the event tree. If no U.S. data was found, global data was used.

A review paper recently summarized multiple sources that give accident frequencies in tunnels for multiple countries [12]. The global average accident rate calculated for accidents in a tunnel is 0.19 accidents per million vehicle kilometers (mvkm). This corresponds to a rate of 0.31 accidents per million vehicle miles (mvm). This frequency (0.31 per mvm) is used as the initiating event in the event sequence diagram.

This frequency normalizes crash data over both the number of vehicles and the miles driven per vehicle. This makes direct comparisons possible. In order to estimate the number of crashes per year expected in a particular tunnel, this frequency is used along with the length of the tunnel and the number of vehicles per year that use the tunnel. For example, if a 1.5-mile-long tunnel has 2 million vehicles use it every year, then using the above accident frequency of 0.31 per mvm, that tunnel should expect 0.93 accidents per year (0.31*1.5*2).

3.1.2. Severity of Accident

Once an accident in a tunnel has been established, the next question is the scale of accident to determine if the hydrogen plays a role in the consequence of the accident. Using another traffic accident road study from Norway, the severity of an accident within a tunnel was determined for 499 person injury accidents where there were 562 unique injuries or fatalities (possible multiple injuries/fatalities per accident) [13]. For the purposes of this analysis, minor accidents consist of slight injuries and severe accidents consist of a fatality or serious injuries. The presence of injuries was used as a marker to indicate a more severe accident because this data was deemed more appropriate and more available than using property damage values as the indicator for a severe accident. Out of the 562-person injury accidents, 465 were minor accidents (82.7%) and 97 were severe accidents (17.3%). In the study, it was determined that the proportion for severe accidents in tunnels is higher than for road accidents. [12, 14]These values were added in the event tree to separate events by severity.

3.1.3. Fire Post-Accident

The next branch of the event tree describes the likelihood of an accident causing a fire. This pertains to fires related to traditional hydrocarbons that are present in gasoline or diesel powered vehicles. Because there are so few FCEVs in the road, it was assumed than an accident involves at least one traditionally-fueled vehicle. A review paper found that 31.66% of severe accidents in tunnels result in a fire, averaging data from Italy, Norway, and Switzerland [12]. This rate is used in the event tree, along with the complimentary probability (68.34%) of a severe accident not resulting in a hydrocarbon fire.

3.1.4. Hydrogen Release Post-Accident

The next event tree branch analyzes whether hydrogen was released from the hydrogen system in an accident. In order to characterize this probability, published crash test data as used. Five tests were conducted with hydrogen vehicles to determine if hydrogen would be released from the storage tank, documented in [15] and [16]. For three of the tests, a 2009 Honda Civic GX natural gas vehicle was retrofitted with a hydrogen fuel system and was subjected to front, rear, and side crashes, per FMVSS No. 301. The pressures for the Type IV containers were chosen to be those that showed the most damage in container crush tests, for the front and rear crashes used a service pressure of 10% and the side crash was pressurized to 100% service pressure. The front crash caused bending of the low-pressure fuel line but there was no evidence of any leaking. The side crash deformed the vehicle body in the vicinity of the fuel container, and deformed the fuel lines but the tank did not leak and the fuel port was functional following the crash. The rear crash caused extensive damage to the fuel system mounting and deformed much of the plumbing and the tank was abraded in several locations but did not leak.

The other two tests used two sports utility vehicles (SUV) were retrofitted with a hydrogen fuel cell with the container located under the body [16]. One of the tests was a side test from FMVSS No. 301 and the other was a FMVSS 303 rear crash test. The container construction was Type III. The 39-L (0.039 m^3) container for the rear crash test was filled with helium. The 74-L (0.074 m^3) Type III front container for the side crash test was filled with a mixture of 80% helium and 20% nitrogen. The fuel systems in both vehicles held pressure following the crashes although the helium sensor on the active fuel system measured a peak of 0.05% by volume of helium for a duration of 4 s after the impact during the side crash test. The sensor also recorded several instances of 0.05% helium by volume, ranging in duration from one to five seconds, during the one-hour post-crash pressure hold test. The amount of helium measured was so small it would not even be detected by the means of a pressure drop.

In all five tests there was not enough damage to the system for it to leak or release hydrogen. Since there is scarce data for a hydrogen release in a full scale vehicle crash test, a gamma distribution conjugate (Jeffreys) prior was used to account for a half of an event (0.5). Gamma distribution conjugate priors are used when little to no data is available for an event [17]. This means that out of the five events, a half of an event is used to determine the probability of hydrogen being released. This is shown in the event sequence diagram with 90% probability of not releasing hydrogen and a 10% probability of a release.

3.1.5. Pressure Relief Device Release

A hydrocarbon fire from another vehicle involved in an accident can result in a release of hydrogen from the TPRD. The heat from the fire can activate the TPRD, releasing the contents of the hydrogen storage vessel, if the fire is located close enough to the hydrogen tank for the TPRD to reach its activation temperature of nominally 110°C. If the fire is not located close enough to the TPRD to activate it, the hydrogen remains in the tank. It is not known the probability of either of these events occurring because the specifics of an actual accident determine the extent of the fire and the proximity of the vehicle and tank to the fire. Thus, it is assumed that there is a 50% chance of the hydrogen being released due to the TPRD, and 50% chance that no hydrogen is released.

3.1.6. Hydrogen Ignition

The next bifurcation in the diagram is whether hydrogen released from the fuel system (not the tank through the TPRD, this is addressed later) will ignite. For the cases where a severe accident causes hydrogen to be released from the system, an evaluation was made for the probability of ignition. Hydrogen ignition probabilities were derived for the Canadian Hydrogen Safety Program [18] by adapting non-hydrogen ignition values suggested in Cox, Lee, & Ang [19]. These ignition probabilities were used for hydrogen quantitative risk assessment in [20] and to develop NFPA 2 and NFPA 55 separation distances. The ignition probabilities are shown in Table 2.

Table 2: Hydrogen ignition probabilities.

Hydrogen Release Rate (kg/s)	Immediate Ignition Probability	Delayed Ignition Probability
<0.125	0.008	0.004
0.125 - 6.25	0.053	0.027
>6.25	0.23	0.12
Average	0.098	0.049

For the purposes of the event tree, an average of the delayed ignition probabilities was used for the delayed ignition because the actual hydrogen release rate would be incident specific. Based on the tank testing detailed previously, it is most likely that hydrogen released would be small amounts present in the fuel line. Using an average value was conservative and deemed appropriate given the uncertainty involved in quantifying this parameter.

The total, probability of ignition is the sum of the averaged probabilities for immediate and delayed ignition, and is estimated here to be 14.7%. This gives a complimentary probability of 85.3% chance of not igniting.

One exception to these probabilities is the case when there is a severe accident, leading to a post-crash fire, no release of hydrogen from the pressure vessel, but hydrogen released from the TPRD. If the fire was large enough to activate the TPRD which releases hydrogen from the tank, it is assumed to be enough to ignite the released hydrogen immediately, forming a jet flame. Thus, it is assumed that for that particular case, there is a 100% chance of ignition, and 100% chance of immediate ignition. Note that separate branches are not shown for the cases of 0% probability.

3.1.7. Immediate versus Delayed Ignition

The final branch of the event tree involves determining when released hydrogen would be ignited. An ignition is typically divided into immediate ignition events and delayed ignition events for hydrogen. Immediate ignition occurs if the leak is ignited within the first few fractions of a second after the leak occurs and delayed ignition allows the hydrogen to accumulate and mix with ambient air before being ignited [21].

The ignition probabilities from Table 2 are used to estimate these probabilities. Since the probability of ignition at all is estimated separately, the immediate or delayed ignition probabilities need to be normalized to the case when the hydrogen will ignite. Since the immediate and delayed ignition probabilities are simply combined to determine the probability of ignition, the normalization must be done by this total probability of ignition. Therefore, the probability of an

immediate ignition (given that an ignition will occur) is 66.67%, and the complimentary probability of delayed ignition is 33.33%.

3.2. Event Sequence Diagram Discussion

Each of the scenarios identified in Figure 4 is presented in Table 3 along with notes assessing whether the respective scenario warranted further characterization with heat transfer and computational fluid dynamics (CFD) models.

Table 3: ESD scenario analysis.

Scenario (from Figure 4)	What Can Happen?	How Likely is it, Given an Accident Occurs?	What are the Consequences?	Notes
A	A FCEV is involved in a minor crash in a tunnel.	Probability of 94.1%. This is the greatest likelihood.	No additional consequence. The tank is expected to survive intact, holding pressure and without leaking.	No modeling needed to analyze this scenario.
B	A FCEV is involved in a severe crash. No hydrogen is released and there is no external fire.	Probability of 3.65%.	No additional consequence. The tank is expected to survive intact, holding pressure and without leaking.	No modeling needed to analyze this scenario.
C	A FCEV is involved in a severe crash. There is no external fire, hydrogen is released from the pressure vessel, but does not ignite.	Probability of 0.35%.	A fuel line break is most likely because of the robustness of the tank. This is downstream of the pressure regulator, limiting released hydrogen to <100 psi (< 0.69 MPa). In this scenario, there is no ignition of hydrogen due to dilution below the flammable limit.	Given the automatic shut-off which closes in an accident and the limited amount of hydrogen released, no modeling will be performed for this scenario.
D	A FCEV is involved in a severe crash. There is no external fire, hydrogen is released from the fuel system and ignites immediately.	Probability of 0.04%.	A fuel line break is most likely because of the robustness of the tank. This is downstream of the pressure regulator, limiting released hydrogen to <100 psi (< 0.69 MPa). The hydrogen ignites immediately.	Given the automatic shut-off which closes in an accident and the limited amount of hydrogen released, no modeling will be performed for this scenario.
E	A FCEV is involved in a severe crash. There is no external fire, hydrogen is released from the fuel system and has a delayed ignition.	Probability of 0.02%. This is the second-least likely scenario.	The consequence depends on the amount of hydrogen released and ventilation rate of tunnel which acts to dilute the concentration of hydrogen.	Computer simulations and CFD models can be run. However, the credibility of this scenario is very minor given the robust tank(s) and vehicle crashworthiness requirements noted.

Scenario (from Figure 4)	What Can Happen?	How Likely is it, Given an Accident Occurs?	What are the Consequences?	Notes
F	A FCEV is involved in a severe crash. No hydrogen is released from the fuel system, there is an external fire, but there is no TPRD release.	Probability of 0.85%.	Depending on the relative locations of the fuel system, TPRD, and external fire, an equal probability was assumed for calculating this likelihood If no hydrogen is released, there is no additional consequence.	No modeling needed to analyze this scenario.
G	A FCEV is involved in a severe crash. No hydrogen is released from the fuel system, there is an external fire, and there is hydrogen released from the TPRD.	Probability of 0.85%.	External fire could cause TPRD to vent hydrogen. The GTR requires the TPRD to be pointed at the ground.	The scenario of a TPRD release of hydrogen will be modeled for the worst-case scenario (a flipped vehicle where the TPRD is directed at the ceiling).
H	A FCEV is involved in a severe crash. Hydrogen is released from the fuel system, and there is an external fire. However, the hydrogen does not ignite.	Probability of 0.16%.	Even with an external fire, there is still a significant probability of the hydrogen not igniting, especially if only a small amount is released. If no hydrogen is released, there is no additional consequence.	No modeling needed to analyze this scenario.
I	A FCEV is involved in a severe crash. Hydrogen is released from the fuel system, and there is an external fire. However, the hydrogen does not ignite.	Probability of 0.018%.	A fuel line break is most likely because of the robustness of the tank. This scenario speculates a jet fire from the fuel line break or TPRD. Tanks are expected to survive severe accidents intact and able to hold pressure.	The TPRD release (similar to the worst case of this scenario) will be modeled in Scenario G.
J	A FCEV is involved in a severe crash. Hydrogen is released from the fuel system and there is an external fire. The hydrogen is not ignited immediately.	Probability of 0.092%. This is the smallest likelihood.	The consequence depends on the amount of hydrogen released from the small fuel lines and ventilation rate of tunnel which acts to dilute the concentration of hydrogen.	Computer simulations and CFD models can be run. However, the credibility of this scenario is very minor given the robust tank and vehicle crashworthiness requirements noted.

Scenario E describes the scenario where an FCEV is involved in a severe crash, hydrogen is released, there is no external fire but the hydrogen ignites anyway, but not immediately. Similarly, Scenario J describes the scenario where an FCEV is involved in a severe crash, hydrogen is released, and there is an external fire but the hydrogen is not ignited immediately. These scenarios have a varied consequence due to the amount of hydrogen released. The tank is designed to survive a severe crash scenario (see Section 2.1) so the credibility of a tank rupture is extremely limited. In a crash, sensors on the vehicle detect the forces associated with the crash and a fail-safe interlock operates a shut-off valve located inside the tank. This limits the hydrogen released to the amount that is contained in the fuel line, if that tubing is damaged in the crash. The most likely consequence

for these scenarios is that a fuel line leak releases hydrogen, however since the amount of hydrogen in the fuel line is minimal the consequence would be a brief combustion of the fuel that generates no overpressure.

Given an accident in a tunnel, the probability of each of the branch line scenarios occurring is shown in Figure 5 as a pie chart. Because the sum of probabilities for all the branch lines equals 1 (and the sum of the branch line frequencies equals the initiating event (accident in a tunnel) frequency), a pie chart is a useful tool to illustrate the relative probability of all the possible scenarios. The colors used in the pie chart correspond to the event tree where green is used to indicate that the hydrogen does not contribute to the severity of the consequences. In all scenarios where the hydrogen remains sealed in the FCEV system or, if released, is vented without igniting, the pie chart is green. Yellow is used to indicate that the hydrogen ignites and contributes to the severity of the incident. Red is used to indicate a catastrophic event, however, the size of the pie slices for these two events is so rare, that the red color is not apparent. As shown, Scenarios A, B, C, F, and H, where there is no additional consequence due to the hydrogen FCEV, clearly dominate the probability of scenarios. Given the resulting branch line probabilities, it was only deemed necessary to characterize the consequences of Scenario G (yellow pie sliver) further.

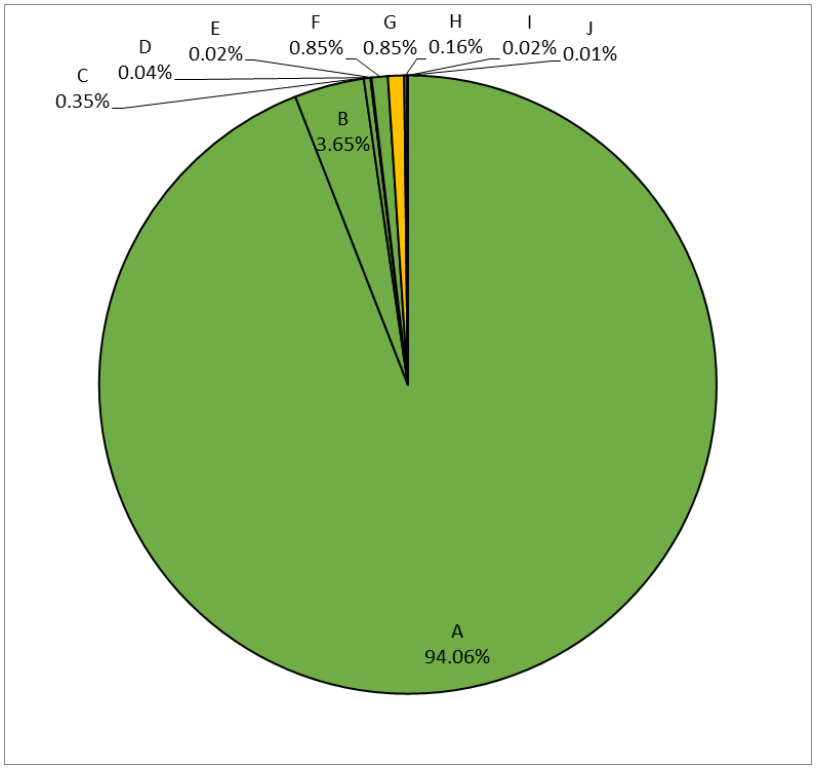

Figure 5: Distribution of probabilities for possible scenarios of outcomes given that a vehicle crash has occurred.

4. MODELING RESULTS

4.1. Pressure Relief Device Activation Analysis

One scenario identified for further analysis was the situation where a hydrogen vehicle is in an accident and is exposed to a resulting fire, Scenario G from the event tree. In this event, it is expected that a jet flame will result as the hydrogen is vented from the tank. This section provides estimation calculations using reduced-order models and simple energy release calculations based on material properties. Detailed modeling efforts are presented in Section 4.2.

For the purposes of this analysis, a typical hydrogen FCEV is considered. The vehicle has a 125-liter (0.125 m^3), 70 MPa tank of hydrogen with a typical TPRD orifice of 2.25 mm. Values for the orifice size of the TPRD vary up to 6 mm, but this analysis uses the smallest orifice size because it results in the longest vent duration, and thus the most conservative case. It should also be noted that the number of hydrogen storage tanks can vary, but the total capacity is roughly 5 to 6 kilograms in a passenger vehicle. The single tank case represents the most conservative situation because all the hydrogen would be released from the single tank when the TPRD activates. When the TPRD releases hydrogen, the pressure in the cylinder decreases quickly. Figure 6 illustrates the rate of hydrogen released decreasing with time as the pressure in the pressure vessel (e.g.-onboard storage tank) decreases. Also shown is the corresponding decrease in the height of the visible flame length. The time to vent all the hydrogen from the tank in this scenario is approximately 300 seconds.

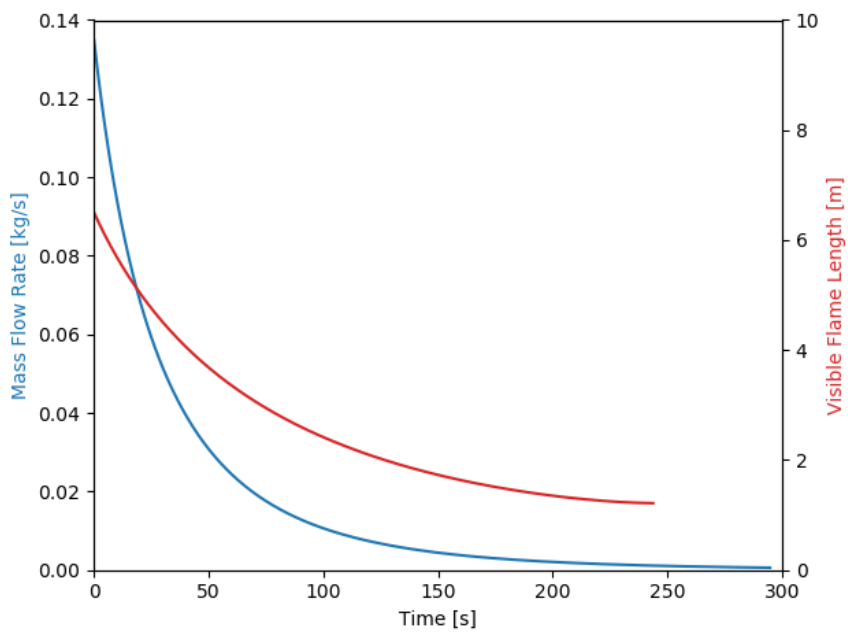

Figure 6: Blowdown of 125 L (0.125 m^3) hydrogen tank showing mass flow rate and visible flame length.

As shown in the graphs, the bulk of the hydrogen is released quickly, the majority within the first minute. The TPRD is designed to face the ground so if a release were to occur it would only impact the ground and not the structure of a tunnel. However, if the vehicle flips over in a crash, the TPRD

would be pointed toward the ceiling of the tunnel. When this release ignites, it will lead to a jet flame that will burn for the time it takes the hydrogen tank to depressurize, around 300 seconds, with the highest flames occurring during the first minute. The worst-case scenario, where the TPRD is facing the ceiling, was first analyzed for both HRR and temperature profiles.

4.1.1. Heat Release Rate Calculations

The height of the tunnel was assumed to be a constant 5.18 m and the flame source is located at 1.25 m from the ground (the height of a vehicle that is flipped over). The combustible components in all passenger vehicles are the same as a hydrogen vehicle; namely: tires, seats, plastic components. A hydrogen vehicle differs from a gasoline vehicle in the energy source (gasoline versus hydrogen). Experimental results for electric vehicles found the peak HRR to range from 4.2 MW to 4.7 MW [22]. NFPA 502 provides a representative HRR for a typical (gasoline) passenger vehicle of 5 MW, which it will reach in approximately 10 minutes. The 4.2 MW value will be used to represent the common combustibles present in a hydrogen vehicle because a FCEV is typically equipped with a small battery unit. In order to complete the fire curves, a quadratic curve was used to illustrate the fire growth and decay, based on [22]. The hydrogen vehicle's HRR is based on the HRR of an electric vehicle plus the HRR of a hydrogen jet fire from the TPRD. This coupling of the HRRs for a FCEV is complicated by the fact that the traditional combustibles like the seats, tires and plastic trim all result in a sooty hydrocarbon flame whose primary means of heat transfer is through radiation to the surrounding surfaces. The hydrogen flame radiates very weakly and its primary means of heat transfer is the hot post-flame gases impinging on a surface. However, for this initial analysis, this approximation is sufficient. The HRR from the jet flame was calculated based on the tank blow down mass release rate using SNL's Hydrogen Risk Assessment Model software (HyRAM) [23]. The mass release rate was used to calculate the instantaneous HRR for the duration of the blowdown using the equation:

$$\boldsymbol{Q = \dot{m} \cdot \Delta Hc} \qquad \textbf{Equation 1}$$

Where Q is the HRR (kW), $\dot{m}$ is the mass flow rate (kg/s) and ΔHc is the heat of combustion of hydrogen (kJ/kg). Figure 6 also illustrates a diesel bus with a peak HRR of 30 MW for comparison, corresponding to values given in both NFPA 502 and [22].

These vehicle HRR values are compared to a 200 MW fire curve, based on the peak HRR results seen in the Runehamar tunnel tests (Figure 2). A 200 MW fire curve is smaller than the 300 MW fire that the RWS fire curve is based on, but was selected because it resulted in surface temperatures at the tunnel ceiling comparable to temperatures in the RWS curve (1,200°C to 1,400°C). An ultra-fast fire curve was used to characterize the growth of the 200 MW fire curve, using the equation:

$$\boldsymbol{Q = \alpha t^2} \qquad \textbf{Equation 2}$$

where Q is the HRR (kW), t is time (s), and α is the fire-growth coefficient (kW/s^2) [23]. An ultra-fast fire growth coefficient (0.19 kW/s^2) was utilized because it corresponds to the fire growth observed in a gasoline pool fire [23] (i.e. flammable liquid) and to the approximate time to peak HRR in Figure 2.

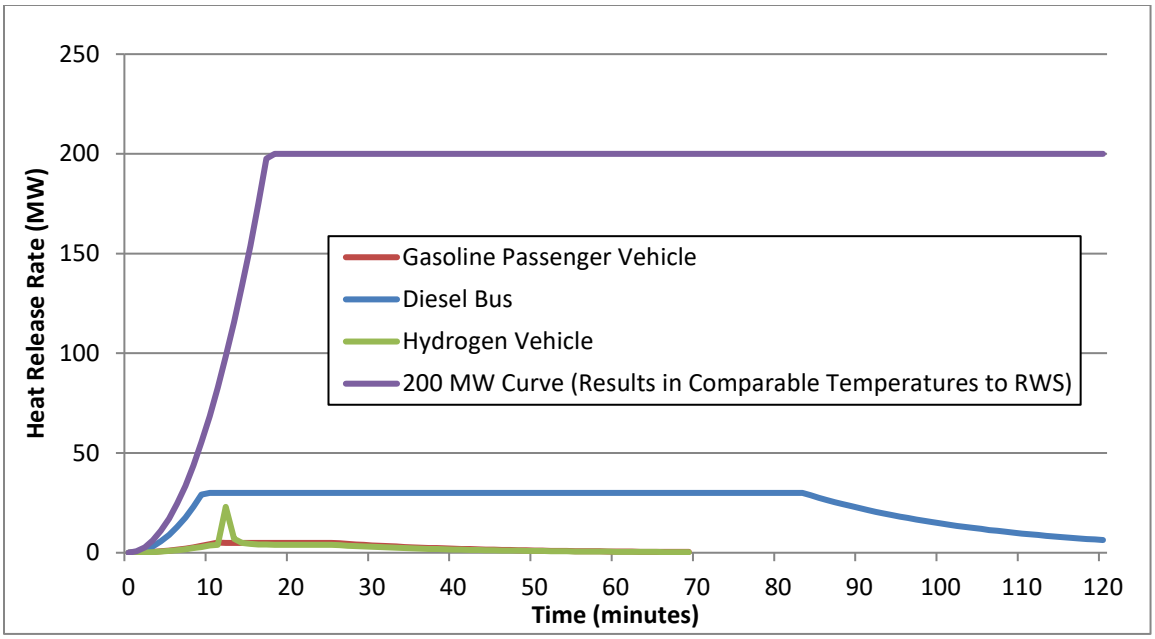

Figure 7: Comparison of gasoline passenger vehicle, hydrogen vehicle, diesel bus and the 200 MW curve.

Figure 7 illustrates that a hydrogen vehicle fire has a peak heat release rate of around 19 MW (corresponding to the hydrogen jet) which is smaller than the 200 MW value caused by a Heavy Goods Vehicle (HGV) and the 30 MW value caused by a diesel-powered bus. Because the peak HRR is less and the fire duration is shorter, a hydrogen vehicle fire would release less heat than most of the HGV tests (Figure 2).

4.1.2. Temperature Calculations

The temperature at the tunnel ceiling for a hydrogen vehicle fire was also compared to a gasoline vehicle fire and the RWS curve, illustrated in Figure 8. The temperature of the gasoline vehicle fire is dominated by radiative heat transfer to the ceiling from the HRR calculated above and correlated using Alpert's correlations for the temperature at the ceiling in a jet fire [24]:

$$T_{max} - T_{\infty} = \frac{16.9Q^{2/3}}{H^{5/3}} \qquad \textbf{Equation 3}$$

where T_{max} is the maximum temperature of the jet at the ceiling (°C), T_{∞} is the ambient temperature (°C), Q is the HRR (kW), and H is the height from the fuel source to the ceiling (m). The peak gasoline vehicle fire temperature derived in this calculation is around 340°C. This gasoline vehicle temperature is within temperatures seen in large scale road tunnel fire experiments, ranging from 110-480°C [25].

The HyRAM output indicates that the hydrogen jet flame temperature is 1,900°C, but only occurs for 39 seconds and dominant heat transfer is convection from the impinging plume of post-flame gases, as shown in Figure 8. The reported values are the temperature at the ceiling above the hydrogen vehicle. For the first 45 seconds, the flame reaches the ceiling, so the reported value is

the flame temperature. After that, the temperature is calculated from the heat flux (q''_{rad}), obtained from HyRAM. The following equation was used to solve for the flame temperature T_f:

$$T_f = \sqrt[4]{q''_{rad}/\varepsilon\sigma} \qquad \textbf{Equation 4}$$

where ε is the flame emissivity (1 black body), and σ is the Stefan-Boltzmann constant.

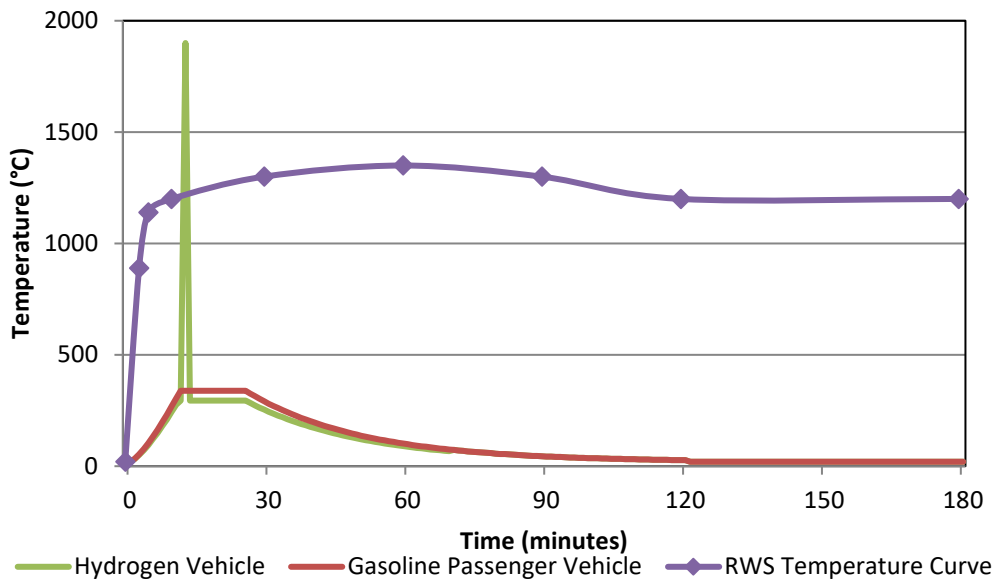

Figure 8: Gas temperatures at the ceiling of the RWS fire curve, a gasoline passenger vehicle and a hydrogen vehicle.

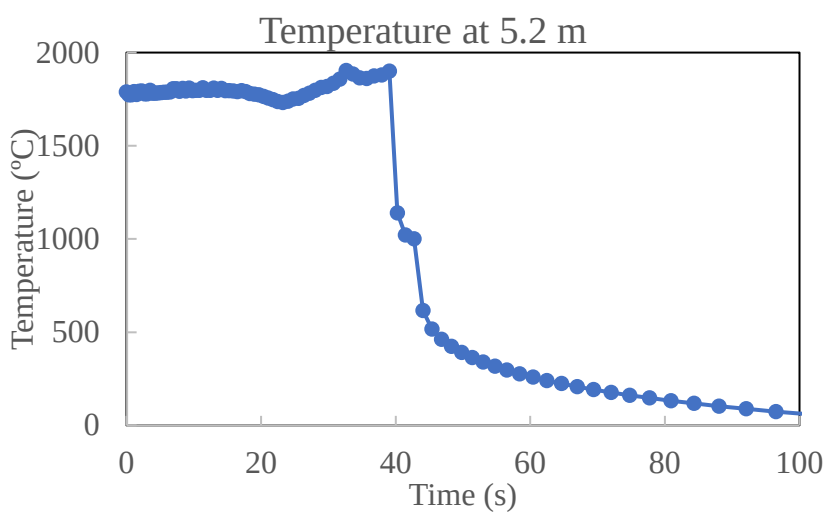

Figure 9: Gas temperature at the ceiling due to a hydrogen vehicle fire for the first 100 seconds.

4.1.3. One Dimensional Transient Model – Stainless steel structure temperature

The goal of this study was to determine if the stainless steel structure supporting the roof concrete panels can reach the epoxy melting temperature ($T_{e,m}$= 140°C) or degradation temperature ($T_{e,d}$ = 90°C) after being exposed to the hydrogen flame. A one dimensional (1D) transient model was developed to calculate the temperature of the stainless steel structure. The stainless steel structure includes the steel bars, rods, plates, and bolts, and it was assumed to be one lumped mass. By conducting an energy balance on the stainless steel structure, the following equation was derived:

$$\dot{E}_{st} = q''_{rad} A_{s,f} + q''_{conv,f} A_{s,f} - q''_{conv,air} A_{s,amb} \qquad \textbf{Equation 5}$$

where $\dot{E}_{st}$ is the energy stored by the steel structure, q''_{rad} and $q''_{conv,f}$ are the flame radiative and convective fluxes on the impingement surface area $A_{s,f}$, and $q''_{conv,air}$ is the convective flux from the steel structure surface area $A_{s,amb}$ to the environment. Using heat flux expressions for each of the terms, the following equation is obtained:

$$(\rho c_p V)_{ss} \frac{dT_{ss}}{dt} = \varepsilon\sigma A_{s,f}(T_f^4 - T_{ss}^4) + h_f A_{s,f}(T_{ss} - T_f) - h_{air} A_{s,air}(T_{ss} - T_{air}) \qquad \textbf{Equation 6}$$

where ρ is the stainless steel density, c_p is the stainless steel specific heat, and V is the volume of the stainless steel structure. The flame temperature shown in Figure 9 was used for T_f. The heat transfer coefficient of the flame was assumed to be h_f = 30 W/m^2-K, and the heat transfer coefficient of air was assumed to be h_{air} = 5 W/m^2-K. The temperature of the stainless steel structure, T_{ss}, was calculated as a function of time. It is important to mention that this model did not account for the ventilation system in the tunnel, and it does not solve for the temperature gradients within the steel structure.

Figure 10(a) shows the stainless steel structure temperature (blue line) as a function of time. The stainless steel structure temperature increases by 3°C. The epoxy melting temperature (140°C) was plotted, red-dashed line for comparison. The stainless steel structure temperature is barely affected by the flame even though the flame temperature reaches a maximum of 1,900°C. As shown in Figure 9, it does not last long enough (~40 seconds) to significantly heat up the stainless steel structure. In addition, the stainless steel structure has a high thermal capacitance (C_t), which slows down the heating process.

$$C_t = (\rho c_p V)_{ss} \qquad \textbf{Equation 7}$$

It was assumed that the stainless steel thermal conductivity is high enough that there are no temperature gradients within the stainless steel structure. However, this assumption might be oversimplifying the problem because the stainless steel structure volume is large compared to the time and size of the hydrogen flame. For a more conservative estimation while still using this simple 1D transient model, the same analysis was done assuming that the heat only affects a section of the structure which is 1/3 of the total structure. Specifically, the length of the stainless steel bar was 4 m long instead of 12 m long, and there were 4 hangers instead of 12.

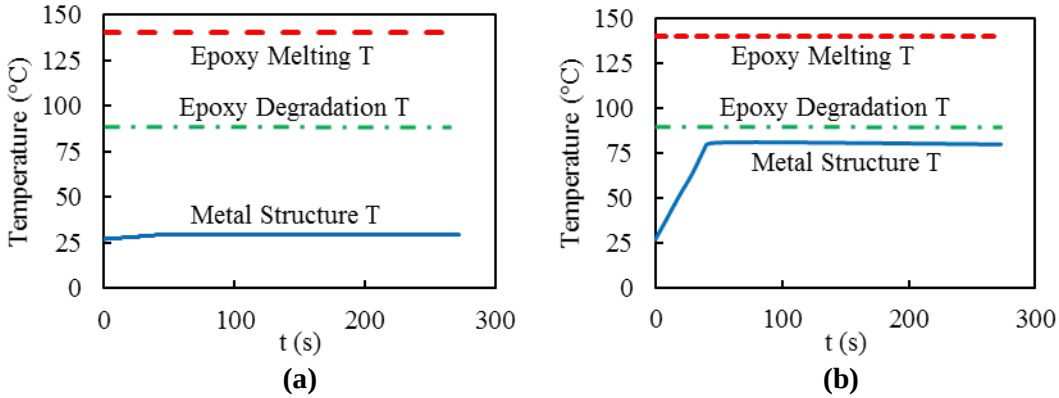

Figure 10: Bulk temperature of stainless steel structure as a function of time for (a) the whole structure and (b) 1/3 of the structure.

The temperature of the smaller structure is shown in Figure 10b (blue line). The stainless steel structure temperature increases to ~80°C at 50 s. After 50 s, the flame temperature at the ceiling surface has decreased dramatically, so the stainless steel structure temperature starts to slowly decrease. The epoxy melting temperature was plotted (red-dashed line in Figure 10(a) and (b)) for comparison. This result shows that even if the hydrogen flame is only heating up 1/3 of the structure, it is not able to increase the stainless steel structure temperature to the melting or degradation temperatures of the epoxy.

From these two calculations, it was concluded that the duration of hydrogen flame is too short to increase the stainless steel structure temperature to the epoxy degradation temperature. The high lumped thermal capacitance of the stainless steel bars that hold the concrete panels causes the structure to heat more slowly. The hydrogen flame extinguishes before elevating the stainless steel structure temperature to temperatures which might be of concern. It is important to remember that the temperature gradient within the solid was not calculated, and the ventilation system was ignored. Ventilation would only decrease the temperature of the stainless steel structure. However, it should be noted that the calculation of only 1/3 of the structure (Figure 10b) resulted in a much higher temperature, meaning local surface temperatures can be higher still. Furthermore, it is noted that while the temperatures calculated are below the epoxy melting temperature, degradation of the epoxy can occur at temperatures as low as 90°C, very close to the calculated temperatures. As such, a more detailed model is necessary to better understand this scenario.

4.2. Numerical Simulations of Fire Scenarios in Tunnel

4.2.1. Introduction

More detailed modeling was done to determine if FCEVs might cause significantly more harm to tunnel structures than conventional vehicles. Three Boston tunnels with different structure configurations (Figure 11) were investigated: the Central Artery North Area (CANA) Tunnel, the Ted Williams Tunnel, and the Sumner Tunnel. As shown in Figure 11a, the CANA Tunnel has a concrete roof. For this tunnel, it was of interest to determine the possibility of explosive spalling due to rapid temperature increase on the concrete roof. The Ted Williams Tunnel and the Sumner Tunnel have concrete panels supported by steel hangers as shown in Figure 11b. The steel hangers are attached to the tunnel roof with bolts anchored in epoxy as shown in Figure 12. While explosive

spalling of the concrete is still a concern on the Ted Williams and Sumner Tunnels, the steel hangers add two more concerns: the distortion of the steel framing that supports the concrete panels, and the performance of the epoxy under the anticipated temperature increase. A loss of strength on the steel hangers at high temperatures could cause the hangers to break, letting the concrete panels fall onto vehicles. The epoxy melting temperature is 140°C; however, its performance starts to deteriorate at around 90°C [26], which could result in the suspended concrete ceiling detaching from the tunnel roof collapsing onto vehicles. While the 1D analysis shown in Section 4.1.2 indicates that the epoxy would not reach melting temperatures, this more detailed 3D analysis can provide more insights into the behavior of the ceiling structure during a fire. The Sumner and Ted Williams Tunnels have very similar ceiling structures, so the simulations were not repeated for the Sumner Tunnel.

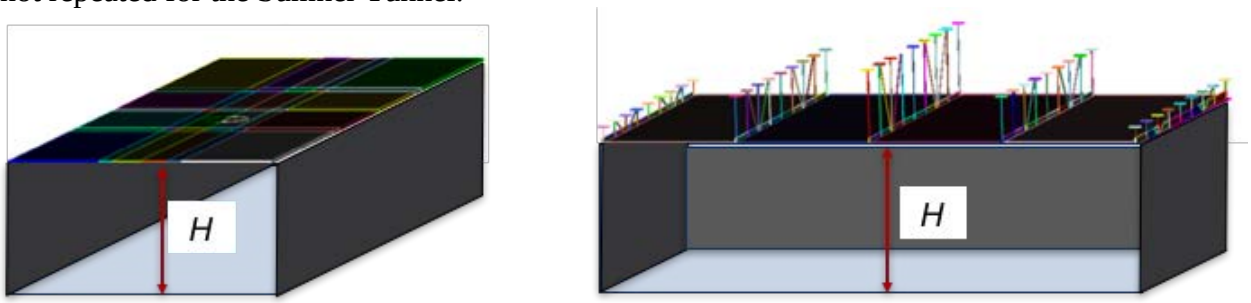

a) b)

Figure 11: Tunnel structure configurations for a) CANA Tunnel and b) Ted Williams and Sumner Tunnels.

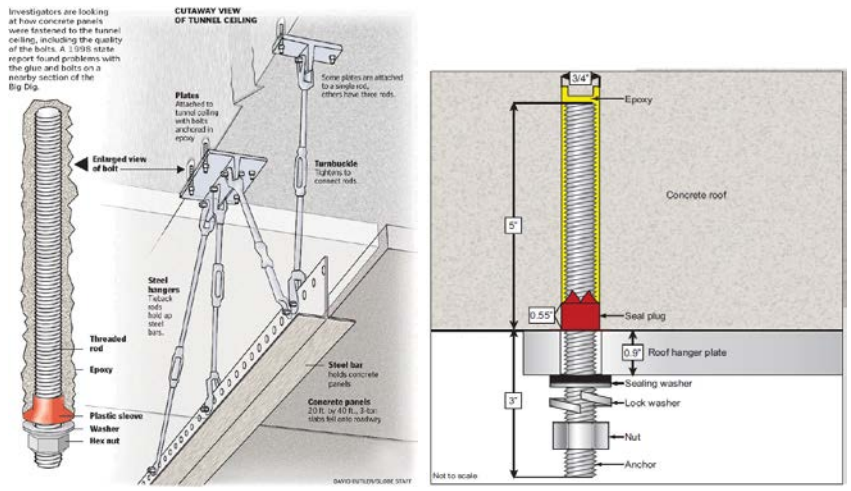

Figure 12: Ted Williams Tunnel cutaway view of tunnel ceiling structure [27].

4.2.1.1. Concrete Explosive Spalling

Concrete spalling is the mechanism through which concrete layers break off from the structural member. It is most likely to happen when the concrete is exposed to high temperatures for a long period of time. Explosive spalling is a concern even for gasoline vehicle fires. The American Concrete Institute provides no guidance for determining spalling (ACI 216.1-97) [28]. The European Codes and Standards for the design of concrete structures (Eurocode 2) indicate that

fire-induced spalling in concrete is unlikely to occur when the moisture content in concrete is lower than 3% [29]. Research on concrete fire-induced spalling has demonstrated contradicting results for the mechanisms that drive spalling [30-34]. It was previously believed that concrete explosive spalling was mostly dependent on the concrete water content. However, researchers have recently shown that spalling is mostly driven by the thermal expansion of the concrete, not the initial moisture content [28, 35]. To illustrate this, Zhao et al. [35] compared the elastic strain energy in specimens with 0% and 90% initial moisture content as shown in Figure 13. The strain energy increment due to the vapor pressure is only 12.6% of the total elastic strain energy when spalling occurs. It was also shown that explosive spalling is highly dependent on the permeability and tensile strength of the concrete. Concrete with low permeability or low tensile strength has higher probability of explosive spalling [36].

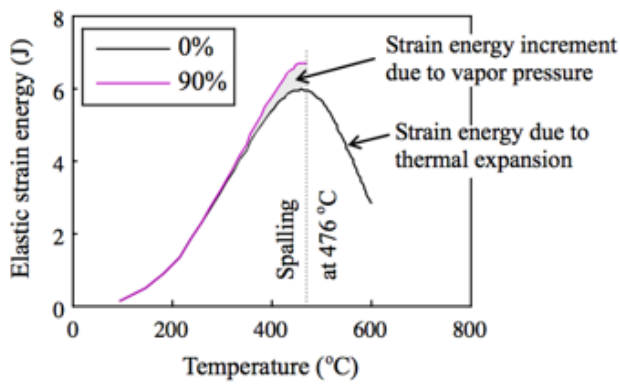

Figure 13: Elastic strain energy as a function of temperature for concrete with 0% humidity and 90% humidity [35].

In the analysis presented in this paper, only the thermal expansion of the concrete was calculated since it is the major factor in concrete spalling. The results were then compared to experimental results from Ali et al. [37]. Ali et al. tested the performance of concrete slabs under ISO 834 and hydrocarbon fire curve heating regimes shown in Figure 14, and reported the observed spalling. The authors started to observe concrete spalling after 15 minutes for the ISO 834 heating test and 2 min for the hydrocarbon heating both at a surface temperature of approximately 750°C. Maximum spalling depths of 25 mm and 20 mm were observed for the ISO 834 and the hydrocarbon tests, respectively. The temperature profiles and the deflection of the CANA and Ted Williams Tunnels' concrete structures were compared with results from Ali et al. [37] results to determine the probability of spalling. Both the CANA and Ted Williams Tunnel results show that the thermal conditions may result in localized spalling in the area where the hydrogen jet flame impinges the ceiling. If the ventilation is operating, the maximum temperature is significantly lower, and spalling is not expected to occur.

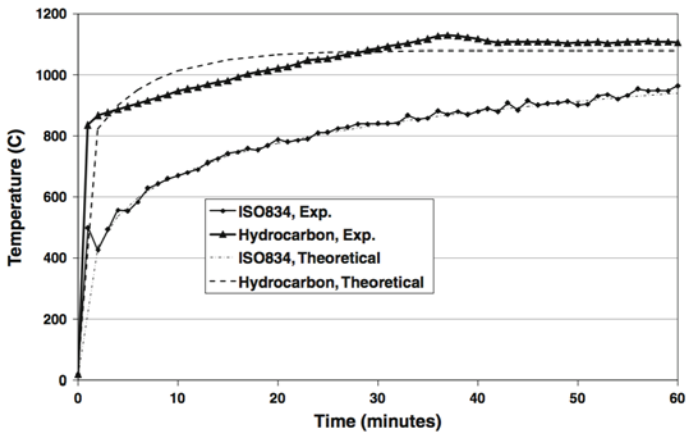

Figure 14: Theoretical and averaged experimental gas temperatures of hydrocarbon and ISO 834 fire curves [37].

4.2.1.2. Yield Stress of Stainless and ASTM A36 Steel

Stainless steel 316 and ASTM A36 yield stress decreases as temperature increases as shown in Figure 15. The general accepted temperature intermittent service temperature for stainless steel 316 is 870°C. The temperature of the steel ceiling structure will increase during a fire in the tunnel. It is important to determine if the steel structure will be able to support the concrete panels during and after a hydrogen jet fire. To determine if the steel structure was compromised by the hydrogen jet fire, the total stress on the steel structure needs will be compared to the yield stress of stainless and ASTM A36 steel at the steel temperature.

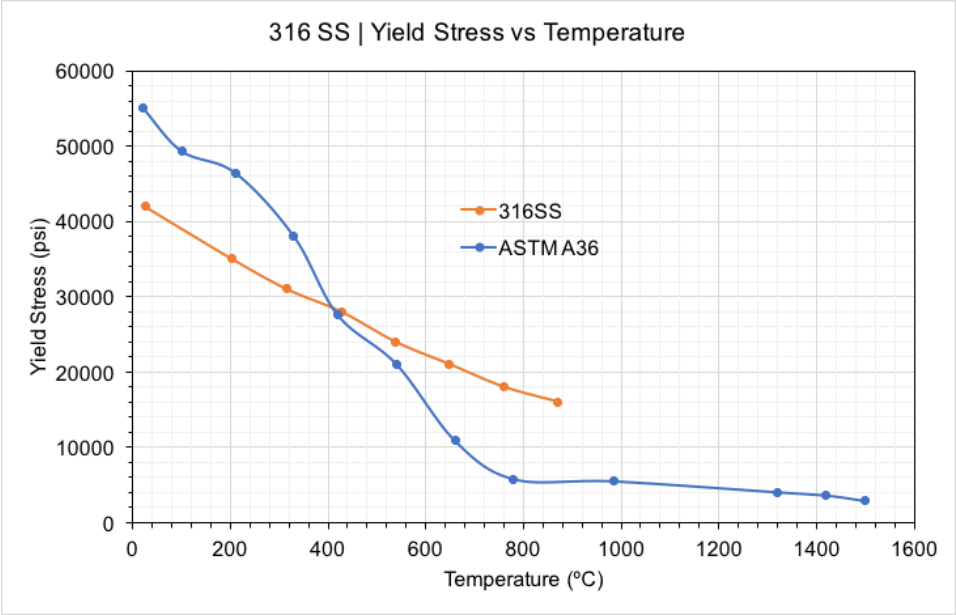

Figure 15: Stainless steel 316 and ASTM A36 steel yield stress decreases as temperature increases. The general accepted temperature intermittent service temperature for stainless steel 316 is 870°C [38].

4.2.1.3. Method Summary

The objective of this study was to predict the thermal expansion of the structural members and the temperature of the epoxy when a hydrogen jet flame impinges on the tunnel ceiling. To this end, the analysis was divided in three different parts: 1) a computational fluid dynamics (CFD) simulation of the flame, 2) a heat transfer simulation of the structural members, and 3) a solid mechanics analysis of the structural members. A Sandia-developed code called Sierra was used to perform the simulations [39]. Sierra is divided into different modules that can interact with each other. The Fuego module [40] was used for the CFD simulation, the Aria module [41] was used for the heat transfer model, and the Adagio module [42, 43] was used to calculate the deflection of the structural members. The CFD simulation provided the boundary conditions for the heat transfer simulation, specifically the radiative and convective heat flux on the tunnel ceiling. These boundary conditions served as input were inputted to Aria to calculate the temperature profiles across the structural members. The temperature profiles on the structural members were input into Adagio to calculate the deflection due to thermal strain on each structural member. The simulations were performed on a SNL high performing computing cluster, Chama, using approximately 152 processors for each run. A simplified analysis was also performed to determine if the stainless steel hangers are able to hold the concrete panels when the hydrogen jet is impinging the stainless steel bar surface.

4.2.2. CFD Simulation of the Fire

A CFD model was created to simulate the fire inside of a tunnel. The model was used to predict the temperature of the hot gases, the heat flux to the tunnel walls, and the velocity field within the tunnel. The Fuego outputs were used as inputs in Aria. Two different scenarios inside the tunnel were explored; specifically, the gas reference temperature, heat transfer coefficient, and the irradiation were calculated. The first scenario simulates two gasoline vehicles on fire. The second scenario simulates a fire started by a gasoline vehicle that spreads to the FCEV and causes the TPRD to open. Figure 16 shows a cross-section of the tunnel used for the CFD simulations where the flow of vehicles is from left to right. Two passenger compact vehicles were positioned in the middle of the tunnel, a hydrocarbon vehicle (left) and an overturned H_2 vehicle (right). The TPRD orifice was located at the top of the overturned H_2 vehicle. The distance between the H_2 release orifice and the ceiling is crucial to predict the temperature of the ceiling structure. Due to the computational time limitations, the CFD modeling of the H_2 jet was performed for one tunnel configuration. The tunnel was assumed to be H = 16 feet 10 inches tall (5.13 meters, CANA Tunnel height) with one traffic lane. The Ted Williams Tunnel and the Sumner Tunnel are 17 feet (5.18 m) and 14 feet (4.27 m) tall, respectively. Sumner's concrete panels are lower than the CANA Tunnel, so higher temperatures should be expected. The simulations were performed with and without ventilation. A laminar flow of 10 mph (4.47 m/s) was assumed for the ventilation with an inlet and outlet as shown in Figure 16. This ventilation rate was designed to be conservative. The CANA Tunnel domain for the hydrocarbon fire consisted of 602,655 elements (628,942 nodes). The CANA Tunnel domain for the H_2 jet flame consisted of 605,080 elements (629,966 nodes).

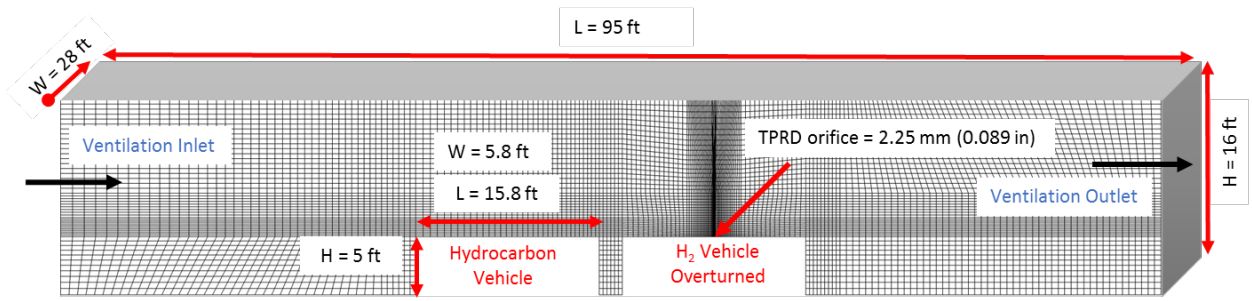

Figure 16: CANA Tunnel and vehicles dimensions, ventilation inlet and outlet, and meshed domain.

4.2.2.1. Mathematical Model

The Fuego module was used for the CFD simulation. Fuego is a robust simulation package capable of simulating highly sooting, buoyancy-driven turbulent-reacting flow dynamics [40]. Fuego uses an approximate projection algorithm with Control Volume Finite Element Method (CVFEM) [44]. Reynolds-Averaged Navier-Stokes (RANS) method was used to solve the time-dependent Navier-Stokes, energy, species, and mass conservation equations. The standard two-equation $\kappa - \epsilon$ closure model was used to evaluate the turbulent eddy viscosity for the RANS simulations. The convection terms in the equations are discretized with a first order upwind differencing technique although the higher order Monotonic Upwind Scheme for Conservation Laws (MUSCL) [45] scheme has also been used for some solutions. Transport equations are solved for the mass fractions of each chemical species, except for the dominant species which is computed by constraining the sum of the species mass fractions to equal one. The ideal gas equation of state is used to relate the density and pressure of the gas mixture. Cantera, a software tool for chemical kinetics, was used to evaluate the species properties [46].

The combustion is modeled with the Magnussen's Eddy Dissipation Concept (EDC) turbulent combustion model [47]. This model uses thermochemistry information, species and state properties, and turbulence kinetic energy and dissipation models to calculate the combustion rates. One limitation of the EDC model in Fuego is that only one fuel can be ignited. It is not possible to simulate the gasoline vehicle and the hydrogen vehicle on fire at the same time, so the hydrocarbon fire was not included in the H_2 jet flame simulations. Instead, the heat flux obtained from the hydrocarbon fire simulations was an input to the boundary conditions in the H_2 jet flame simulations. The high velocity and high temperatures observed in the H_2 jet flame simulations showed that during the 5 minutes of the H_2 jet blowdown, the gasoline vehicle fire effect is negligible compared to the H_2 jet flame effect.

The SNL-developed finite element code Syrinx coupled with Fuego provide the convective and radiative loads [48] needed in the Aria heat transfer model. Syrinx is a discrete ordinate, participating media radiation (PMR) heat transfer solver that uses the Streamwise Upwind Petrov-Galerkin discretization [49]. The turbulent reacting flow field (Fuego) and participating media radiation (Syrinx) field provide the heat transfer coefficient, the gas reference temperature, and the incident radiative flux or irradiation for use in Aria. Fuego uses the total surface heat flux, $\dot{q}'''$, at ceiling structure to calculate the heat transfer coefficient,

$$\dot{q}'''_{cond} = \dot{q}'''_{conv} + \dot{q}'''_{rad} \qquad \textbf{Equation 8}$$

where the convective heat flux, $\dot{q}'''_{conv}$, is defined as:

$$\dot{\mathbf{q}}'''_{\mathbf{conv}} = \mathbf{h}(\mathbf{T} - \mathbf{T_r}) \qquad \textbf{Equation 9}$$

where h is the heat transfer coefficient, and T_r is the gas reference temperature. The radiative heat flux, $\dot{q}'''_{rad}$, is described as:

$$\dot{q}'''_{rad} = \epsilon\left(\sigma T^4 - G\right) \qquad \textbf{Equation 10}$$

where ϵ is the solid emissivity, σ is the Stefan-Boltzmann constant, and G is the incident radiative flux or irradiation. Using a gray body radiative analysis for the hot gas mixture yields a conservative analysis. The surface temperature, T, was approximated by assuming the temperature through a solid thickness to be locally one-dimensional. A constant concrete thermal conductivity of 1.4 W/m-K was used, and a thickness of 4 inches (0.10 m) was assumed for the solid. The surface temperature was approximated in order to calculate the heat transfer coefficient in Fuego. Aria uses the Fuego heat transfer coefficient, and recalculates the surface temperature as explained in Section 4.2.3.1.

4.2.2.2. Initial and Boundary Conditions

At t = 0 seconds, the tunnel was assumed to be at ambient temperature with a zero-velocity field and an air gas composition (79=% nitrogen and 21% oxygen). For the case with no ventilation, the tunnel inlet and outlet were set as open boundaries with a constant ambient temperature and an air gas composition. For the case with ventilation, a constant velocity of 10 mph (4.47 m/s) at ambient temperature was set at the tunnel inlet, and an open boundary condition was imposed at the tunnel outlet. The simulation was run long enough to get a steady flow in the tunnel before starting the fire.

The hydrocarbon fire was simulated as a pool fire where a fuel inlet velocity was applied on and around the vehicles. The boundary conditions for this scenario are described in Section 4.2.2.3. For the hydrogen jet fire, an inlet boundary condition was applied at the TPRD orifice located on top of the overturned vehicle (see Figure 16). The boundary conditions for this scenario are described in Section 4.2.2.4.

4.2.2.3. Hydrocarbon Fire Parameters

The vehicle on fire was simulated as a fuel pool fire using JP8 as the fuel of combustion. The heat release rate of a passenger gasoline vehicle on fire is approximately 5 MW (see). The heat release rate (HRR) is defined as follows:

$$\boldsymbol{HRR = \dot{m}_0 \Delta H_c} \qquad \textbf{Equation 11}$$

where $\dot{m}_0$ is the fuel mass flowrate and ΔH_c is the heat of combustion [50]. Equation 10 was used to calculate the fuel mass flow rate needed to achieve a heat release rate of 5 MW for the gasoline vehicle on fire. The JP8 heat of combustion at 25°C is $\Delta H_c = 45$ MJ/kg fuel, which results in a fuel mass flow rate of $\dot{m}_0 = 0.1$ kg/s. A 20 MW JP8 fire was also investigated, which corresponds to a 4.5 kg/s fuel mass flow rate.

Mangs and Keski-Rahkonen [51, 52] measured the temperatures on and around a gasoline vehicle on fire, so their results were used to validate this numerical simulation.

4.2.2.4. H_2 Jet Fire Parameters

In this analysis, the vehicle has a 125-liter (0.125 m^3), 70 MPa (10,000 psi) tank containing 5 kg of hydrogen with a TPRD orifice of 2.25 mm. The 2.25 mm diameter disk in the TPRD melts at 110°C. It was assumed that the temperature and pressure inside the tank remained constant until the TPRD release happens. This is a reasonable assumption given the H_2 tank thickness and the rapid hydrocarbon fire progression. MassTran (Mass Transport) [53], a network flow modeling tool developed by SNL, was used to calculate the amount and velocity of hydrogen that would be release in the event of the TPRD reaching 110°C needed to activate the valve. MassTran enables users to model compressible and incompressible flows of multi-species gas mixtures through arbitrary arrangements of pipes, vessels, and flow branches [53]. As the tank empties, MassTran calculates the temperature, pressure, mass, and density of the gas in the tank and the mass flow rate and velocity of the released gas. Figure 17 shows the velocity and temperature of the jet over the five minutes that it takes the tank to empty. The maximum release velocity of 918 m/s is at the instant of release. The velocity decreases to 700 m/s after 30 seconds, and the flow remains choked (constant velocity) for approximately 4 minutes. After 4 minutes, the velocity starts decreasing again until the tank is empty. The temperature of the gas inside the tank decreases from ambient temperature to -46°C in the first 30 seconds, and it increases until it reaches ambient temperature at the end of the release.

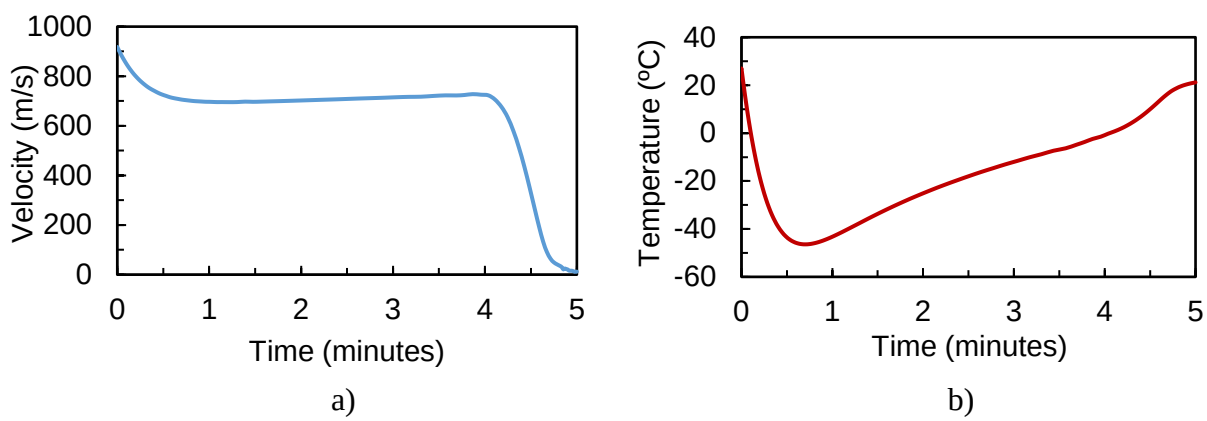

Figure 17: a) H_2 jet velocity and b) H_2 jet temperature as released from a 2.25 mm valve.

The 2.25 mm diameter was adjusted to capture the full size of the tunnel and the five-minute-long simulation in a reasonable amount of computational time. The smallest reasonable diameter that can be modeled is 5.25 cm. A larger release diameter means the mass flow is greater than what

would be expected, and the fire would have a larger total heat release rate (Figure 18) because of the excess fuel being released. To correct the mass flow rate, the velocity can be decreased, but for the heat transfer model, the flame duration of impingement on the ceiling members is important. By decreasing the velocity, the length and duration of the H_2 jet flame would be underestimated, which would result in underestimation of the heat flux at the ceiling of the tunnel. To investigate the worst-case scenario, a release diameter of 5.25 cm with a constant velocity of 700 m/s was assumed.

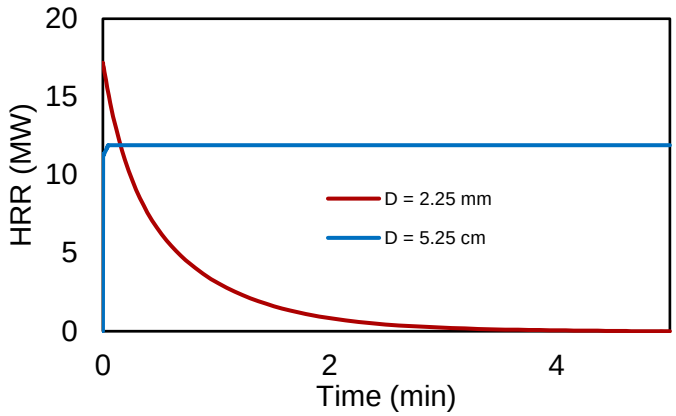

Figure 18: Heat release rate for a hydrogen tank orifice of 2.25 mm and a 5.25 cm.

The H_2 jet was assumed to ignite as soon as the TPRD is triggered, and the H_2 flammability limits are reached. The hydrocarbon fire acts as the ignition source for the H_2 jet. When hydrogen is ignited, it generates superheated steam. The lower and upper hydrogen/air mixture in a turbulent jet flow flammability limits are 0.08 and 0.75 mole fraction, respectively. Experiments by Schefer et al. [54] show that ignition of a turbulent hydrogen jet requires 8% concentration to achieve ignition instead of 4% concentration seen in stagnant mixtures.

A validation study was previously performed by Houf et al. to assesses the model's ability to predict velocity and concentration decay along the centerline of unignited hydrogen free jets and the centerline temperature for laboratory-scale hydrogen jet flames [55]. Houf et al. also validated the model's ability to predict hydrogen dispersion in an enclosed space by comparing the Fuego results with large-scale hydrogen blowdown release experiments [56].

4.2.3. Heat Transfer Simulation of Structural Members

A heat transfer simulation using the Aria module was developed to calculate the temperature profiles of the structural members. The reference temperature, heat transfer coefficient, and the irradiation from Fuego were used as boundary conditions on the surface in direct contact with the heated gases. Two different meshes were used for this study, one for the CANA Tunnel and one for the Ted Williams Tunnel. Figure 19 shows the domain used for the CANA roof concrete slab. The slab is 95 feet (28.96 m) long, 56 feet (17.07 m) wide, and 3 feet (0.91 m) thick. Figure 20 shows the mesh and dimensions used for the Ted Tunnel ceiling structure. The concrete panels are 8 feet (2.44 m) long, 12 feet (3.66 m) wide, and 4 inches (0.10 m) thick. The worst-case scenario was chosen where the flame is located directly below the shortest hanger (1.8-ft (0.55 m) long, 2-in (0.05 m) diameter) of the structure. The roof hanger plates are 10.25×9×0.9 in (0.26×0.23×0.02

m). From this point on, the stainless steel structure composed by the steel bar, the hangers, and the plates will be referred as stainless steel hangers as they were modeled as one domain. The bolts anchored in epoxy were not included in the simulation. Instead, it was assumed that the bolts and the epoxy were at the maximum temperature of top surface of the roof hanger plates. Both meshes were refined at the impingement area to better capture the temperature changes. The CANA and Ted Williams Tunnel ceiling domains consisted of 295,170 elements (328,867 nodes) and 1,159,387 elements (1,420,499 nodes), respectively.

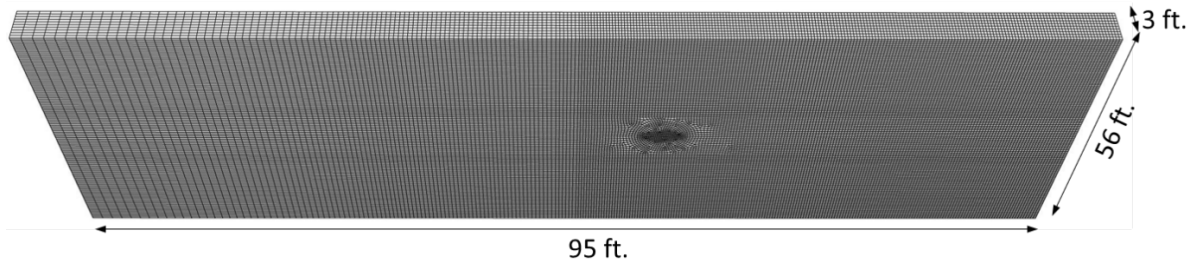

Figure 19: Mesh used for the CANA roof concrete slab heat transfer simulation.

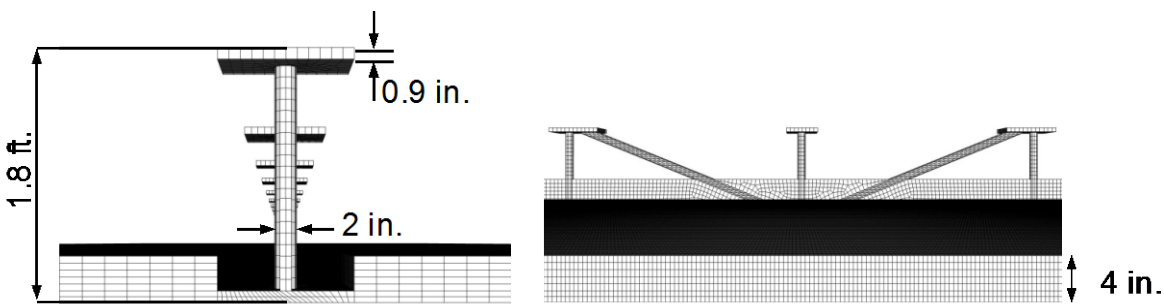

Figure 20: Mesh used for the Ted Williams Tunnel ceiling structure (concrete panels supported by stainless steel hangers and plates) for heat transfer simulation: a) front view, and b) side view.

4.2.3.1. Mathematical Model

Aria was used for the heat transfer model of the ceiling structure. Aria is a Sierra module that performs steady and unsteady thermal analysis of two- or three-dimensional systems that consist of multiple solid materials. Aria solves systems of partial differential equations (PDEs) using the finite element method (FEM). In this study, Aria was used to solve the conservation of energy within the solid to get the solid temperature $T(x, y, z, t)$,

$$\boldsymbol{\rho C_p \frac{\partial T}{\partial t} - \nabla \cdot (k \nabla T) = 0} \qquad \textbf{Equation 12}$$

where ρ is the density, C_p is the specific heat, and k is the thermal conductivity. The Galerkin method was used to discretize in space, and the finite differences method was used to discretize in time.

4.2.3.2. Initial Conditions

The ceiling structure was assumed to be at ambient temperature, T_{amb}, at t = 0 seconds,

$$\boldsymbol{T(t = 0, x) = T_{amb}}. \qquad \textbf{Equation 13}$$

where the ambient temperature was assumed to be 26°C. The whole ceiling structure was assumed to be insulated (worst-case scenario), except for the surface in direct contact with the hot gas plume mixture. Convective and radiative boundary conditions were applied at that surface. The convective flux, $\dot{q}'''_{conv}$, applied to the surface is defined as follow,

$$\boldsymbol{\dot{q}'''_{conv} = h(T - T_r)} \qquad \textbf{Equation 14}$$

where T is the surface temperature, h is the heat transfer coefficient, and T_r is the gas reference temperature. Both h and T_r were Fuego (CFD) outputs (see Section 4.2.2.1 for details). The radiative surface flux, $q_{n,r}$, is the difference between the energy that radiates away and the incident energy, and it is defined as follow,

$$\boldsymbol{q_{n,r} = \epsilon\left(\sigma T^4 - G\right)} \qquad \textbf{Equation 15}$$

where ϵ is the solid emissivity, σ is the Stefan-Boltzmann constant, and G is the irradiation obtained in the Fuego simulation. Equation 11-Equation 14 were solved for the CANA concrete slab, the Ted Williams concrete panels, and Ted Williams stainless steel hangers.

4.2.4. Solid Mechanics Analysis on Structural Members

A solid mechanics model was developed to calculate the deflection on the ceiling structures due to the temperature change inside the solid. The temperature results from the heat transfer model were inputted in the solid mechanics model. The results from the heat transfer and solid mechanics model were then compared to Ali et al. experimental temperature and deflection results. Table 4 shows the differences between Ali et al. experimental setup and the numerical H_2 jet simulations setup, specifically, the dimensions of the concrete slabs, the distance from the fire source to the concrete slab, and the load applied to the concrete slab. The Adagio model uses the same mesh used in the Aria model.

Table 4: Differences between Ali et al. [37] experimental setup and the numerical H_2 jet simulations setup.

Concrete slab	Experimental simulation using hydrocarbon fire curve [37]	Numerical H_2 Jet Simulations
Dimensions	10 ft. 10 in. (3.30 m) long 3 ft. 11 in. (1.19 m) wide 8 in. (0.20 m) thick	95 ft. (28.96 m) long 28 ft. (8.53 m) wide 3 ft. (0.91 m) thick
Distance from fire source	10 ft. (3.05 m)	12 ft. (3.66 m)

Load applied	27 kN	0 kN

4.2.4.1. Mathematical Model for Thermal Deflection

Adagio was used to calculate the thermal deflection of the ceiling structure. Adagio is a Lagrangian, three-dimensional code for finite element analysis of structures. Adagio uses a multi-level iterative solver to effectively solve problems with large deformations and nonlinear material behavior. The code is written for parallel computing environments enabling scalable solutions of extremely large problems.

4.2.4.2. Mathematical Model for Stress Calculations

The total stress on the stainless steel structure was calculated with a simplified one dimensional model. The concrete panels are supported by a stainless steel bar on opposite sides as shown in Figure 21. Each stainless steel structure bears five concrete panels on each side. The weight of each concrete panel is 4,700 lbf (20.90 kN). It was assumed that the stainless steel structure support beam acts like two cantilevers, each supporting 2,350 lbf (10.45 kN) over an 8 ft (2.44 m) length. Figure 21 also shows the total load on the stainless steel structure. The loads are distributed over a length of 8 ft (2.44 m), so every inch of the stainless steel bar supports 24.5 lbf on either side as shown in Figure 22 (equivalent to 4.29 kN/m). It was assumed that the load acts at the far edge to give the largest moment possible. The stress, σ, was calculated with the following equation:

$$\boldsymbol{\sigma = \frac{Mc}{I}} \qquad \textbf{Equation 16}$$

where M is the total moment and c is the distance from midplane. The moment of inertia, I, is defined as,

$$\boldsymbol{I = \frac{bh^3}{12}} \qquad \textbf{Equation 17}$$

where b is the length of the stainless steel bar and h is the thickness of the stainless steel bar. The total stress calculated with equation is $\sigma = 808\, psi$ (5.57 MPa). This calculation can be repeated for the total length of the stainless steel bar (40 feet or 12.19 m), which would result with the same total stress of $\sigma = 808\, psi$ (5.57 MPa). The total stress will be compared to the yield stress of stainless steel at the steel maximum temperature after the 5 minutes of the hydrogen release (results from heat transfer model). If total stress is significantly lower than the yield stress, then the steel structure will be able to support the concrete panels.

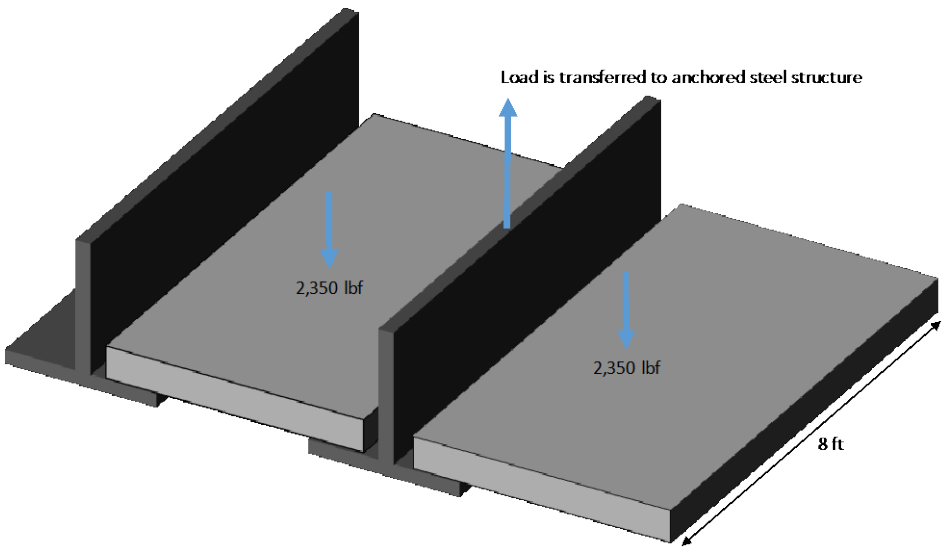

Figure 21: Concrete panels supported by stainless steel hangers. Each stainless steel structure has a load of 2,350 lbf (half of the weight of one concrete panel) in the direction of gravity on each side of the steel bar.

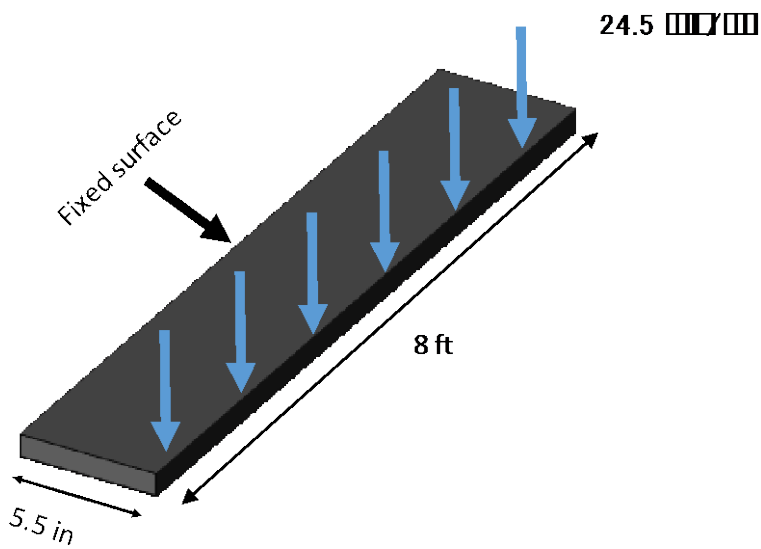

Figure 22: Loads on steel bar are distributed over a length of 8 ft. Every inch of the stainless steel bar supports 24.5 lbf on either side.

4.2.5. Material Thermal Properties

The properties of siliceous aggregate concrete were used in the heat transfer model and the solid mechanics model for both the CANA and Ted Williams Tunnels. Stainless steel 316 properties were used for the Ted Williams hangers and plates, although ASTM A36 steel was also used to analyze yield stress. The density and emissivity were assumed to be constant, and are listed in Table 5.

Table 5: Density and emissivity used in the heat transfer model and/or the solid mechanics model.

	Density (kg/m^3)	Emissivity
Concrete	2,300	0.88
Steel	7,920	0.78

Temperature dependent specific heat, thermal conductivity, and thermal strain were used as specified by Kondur and Sultan [57, 58]. Figure 23 shows the specific heat and the thermal conductivity of the concrete and the stainless steel used in the Aria model. The specific heat and thermal conductivity of stainless steel was assumed constant for temperatures higher than 725°C. Figure 24 shows the thermal strain used in the Adagio model.

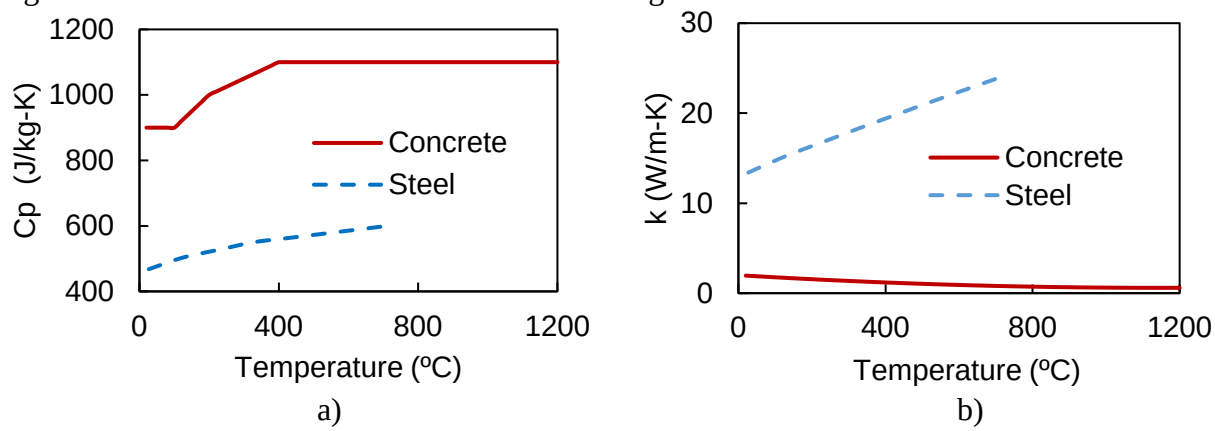

Figure 23: Thermal properties of concrete and stainless steel used in the heat transfer model: a) specific heat and b) thermal conductivity [57].

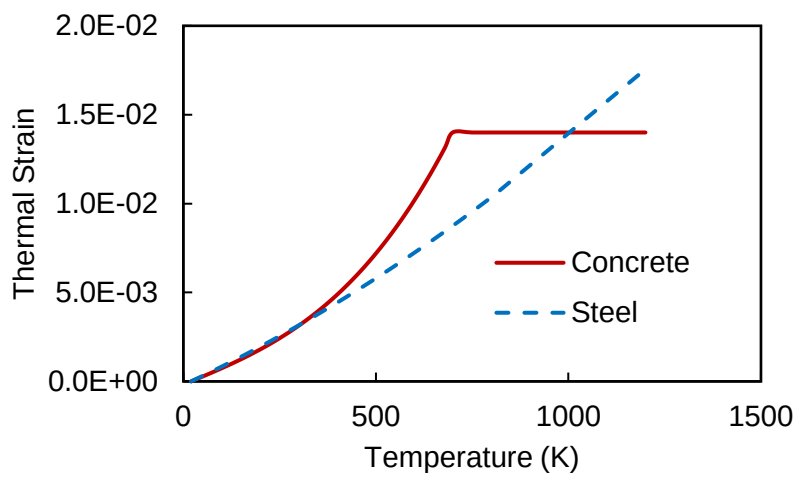

Figure 24: Thermal strain for concrete and stainless steel as a function of material temperature used in the solid mechanics model (Adagio) [58].

4.2.6. Results and Discussion

The results for the 5 MW and 20 MW hydrocarbon-only fires are presented in Section 4.2.6.1 and Section 4.2.6.2, respectively. These simulations were done only for the worst-case scenario where the ventilation is not operating. There is no hydrogen jet flame in these simulations, they were performed in order to assess the relative impacts of the traditional hydrocarbon combustibles resulting from a typical vehicle tunnel accident fire. The hydrogen jet flame simulations are presented in the following sections, and these simulations do not include the hydrocarbon fire (see Section 4.2.2.1). The results from the Fuego, Aria, and Adagio simulations for the CANA tunnel without ventilation are presented in Section 4.2.6.3. The results for the CANA tunnel with ventilation are presented in Section 4.2.6.4. Sections 4.2.6.5 and 4.2.6.6 present the Ted Williams Tunnel with and without ventilation results, respectively. For the hydrogen jet flame simulations, a range of 100°C to 2100°C was used in all the temperature visualizations to compare the different scenarios which lower temperature scales on the graphical images were used for the hydrocarbon-only analyses.

4.2.6.1. 5 MW Hydrocarbon Fire Simulation

Figure 25 is an instantaneous illustration of the heated mixture generated by the 5 MW hydrocarbon fire from the CFD simulation. The traffic flows from left to right, and both hydrocarbon vehicles are positioned in the middle of the tunnel, one behind the other to represent a collision between two vehicles. The hot gas mixture reaches the ceiling in 4 seconds. The system reaches a pseudo-steady state after approximately 2.5 minutes. A maximum gas temperature of 372°C was observed closed to the vehicle surfaces. The simulation was run for 4 minutes to ensure that the heat transfer coefficient, the incident flux, and the reference temperature were not changing with time. The results at 4 minutes were then used for the extent of a one hour hydrocarbon fire.

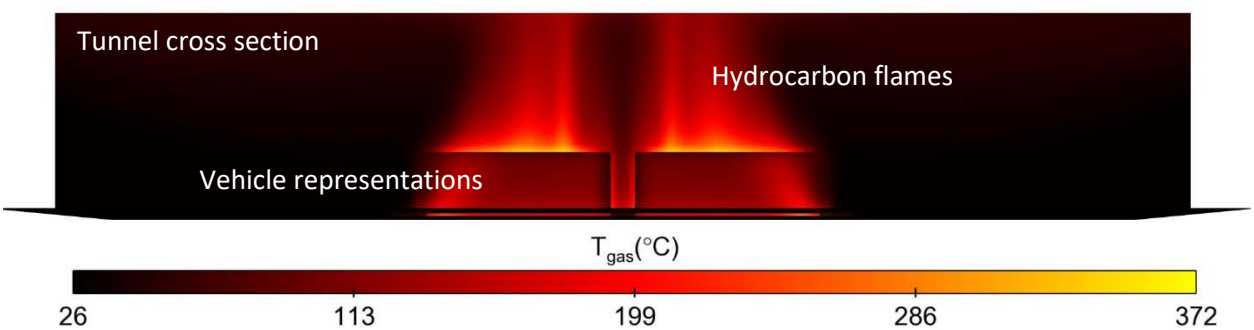

Figure 25: Instantaneous illustration of heated mixture for the 5 MW hydrocarbon fire CFD simulation (no ventilation). A maximum temperature of 372°C was observed closed to the vehicle surfaces.

The maximum gas reference temperature and the maximum concrete temperature are compared in Figure 26. The gas temperature at the ceiling interface reaches a maximum temperature of 170°C at t = 27 seconds. The temperature decreases until it reaches a steady temperature of approximately 139°C at t = 2.3 minutes. The gas mixture at the ceiling interface transfers thermal energy to the ceiling resulting in a gas temperature decrease. In addition, when the heated gas mixture impinges the ceiling surface, mixing with the ambient air is enhanced. A constant gas temperature of 139°C

was used for the remainder of the one hour fire duration. The temperature of the tunnel concrete surface reaches a maximum of 59°C in a 5 MW hydrocarbon fire that lasts one hour. At t = 5 minutes of the 5 MW hydrocarbon, the concrete surface temperature increases only 6°C, which indicates that the effect of the hydrocarbon fire on the concrete structure can be neglected during the 5 minutes of the hydrogen release.

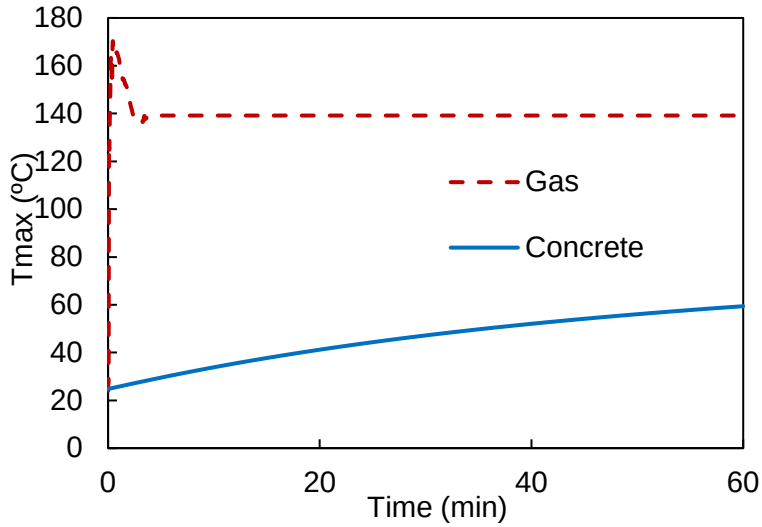

Figure 26: Maximum temperature as a function of time for the 5 MW hydrocarbon fire in the CANA Tunnel with no ventilation of: the gas mixture (dash-red line) and the concrete (continuous-blue line). A temperature difference of 113°C is observed between the maximum temperature of the gas mixture and the maximum concrete temperature.

The temperature variation across the concrete thickness was plotted at the location of the maximum surface temperture as shown in Figure 27. A thermal penetration depth of δ_p = 7.5 inches (0.19 m) is observed where the concrete temperature linearly decreases from 55°C to 25°C. The concrete slab is essentially uninfluenced by the change in surface conditions after the thermal penetration depth, and it remains at ambient temperature.

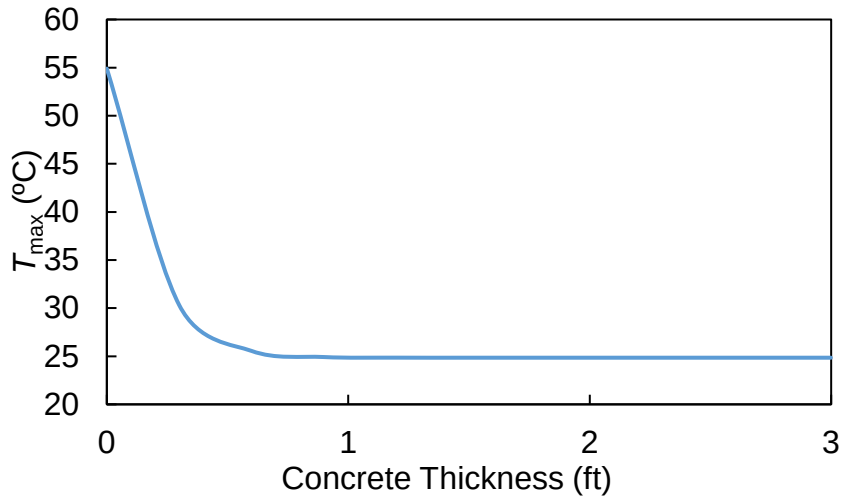

Figure 27: Temperature variation across concrete slab (the location of the surface was chosen at the maximum surface temperature) at *t* = 60 min for the 5 MW hydrocarbon fire inside the CANA tunnel with no ventilation. A thermal penetration depth of δ_p = 7.5 inches (0.19 m) is observed where the concrete temperature linearly decreases from 55°C to 24°C.

4.2.6.2. 20 MW Hydrocarbon Fire Simulation

Figure 28 is an instantaneous illustration of the heated mixture generated by the 20 MW hydrocarbon fire from the CFD simulation. The traffic flows from left to right, and both hydrocarbon vehicles are positioned in the middle of the tunnel, one behind the other to represent a collision between two vehicles. The hot gas mixture reaches the ceiling in 4 seconds. The system reaches a pseudo-steady state after approximately 2.5 minutes. A maximum temperature of 745°C was observed close to the vehicle surfaces, which is 373°C higher than the maximum temperature observed in the 5 MW hydrocarbon fire. The simulation was run for 4 minutes to ensure that the heat transfer coefficient, the incident flux, and the reference temperature were not changing with time. The results at 4 minutes were then used for the extent of a one hour hydrocarbon fire.

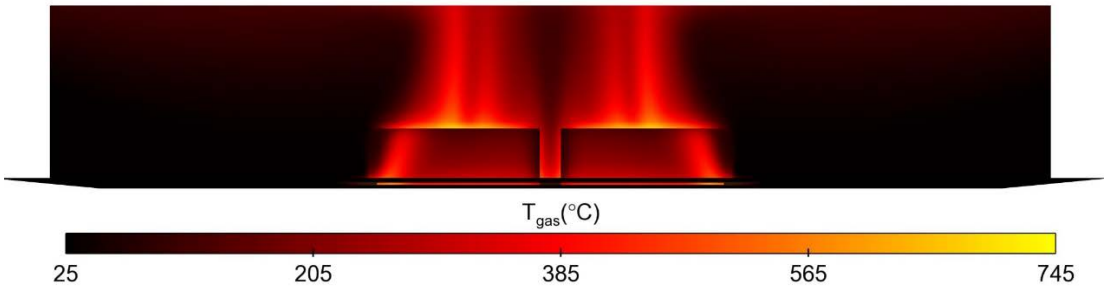

Figure 28: Instantaneous illustration of heated mixture for the 20 MW hydrocarbon fire CFD simulation (no ventilation). A maximum temperature of 745°C was observed closed to the vehicle surfaces.

The maximum gas reference temperature and the maximum concrete temperature are compared in Figure 29. The gas temperature at the ceiling interface reaches a maximum temperature of 401°C at t = 12 seconds. The temperature decreases until it reaches a steady temperature of approximately 342°C at t = 1.4 minutes. The gas mixture at the ceiling interface transfer thermal energy to the ceiling resulting in a gas temperature decrease. In addition, when the heated gas mixture impinges the ceiling surface, mixing with the ambient air is enhanced. A constant gas temperature of 342°C was used for the remainder of the one hour fire. The temperature of the tunnel concrete surface reaches a maximum of 170°C in the 20 MW hydrocarbon fire after one hour, which is 120°C higher than the maximum concrete temperature in the 5 MW hydrocarbon fire scenario. The 20 MW hydrocarbon fire has a greater effect on the surface temperature than the 5 MW hydrocarbon fire; however, compared to the effect of the hydrogen jet flame, the 20 MW hydrocarbon fire can still be neglected during the 5 minutes of the hydrogen release.

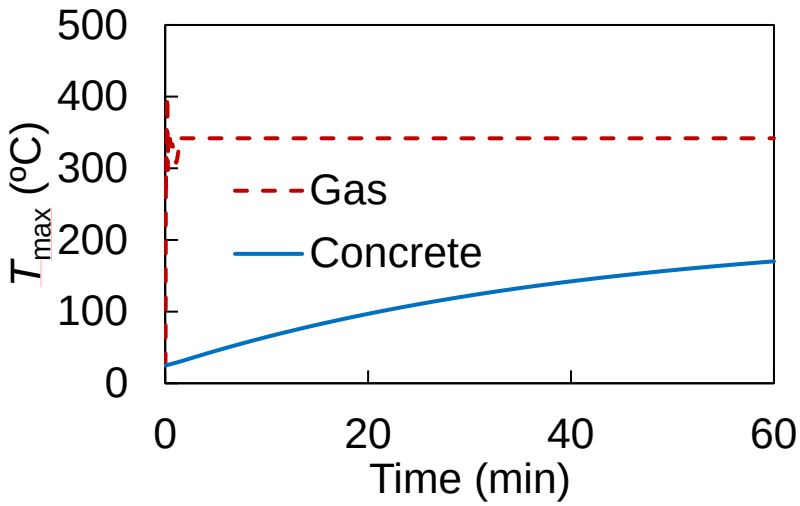

Figure 29: Maximum temperature as a function of time for the 20 MW hydrocarbon fire in the CANA Tunnel with no ventilation of: the gas mixture (dash-red line) and the concrete (continuous-blue line). A temperature difference of 170°C is observed between the maximum temperature of the gas mixture and the maximum concrete temperature after 1 hour of exposure.

The temperature variation across the concrete thickness was plotted at the location of the maximum surface temperture as shown in Figure 35. A thermal penetration depth of δ_p = 7.5 inches (0.19 m) is observed where the concrete temperature linearly decreases from 170°C to 25°C. The concrete slab is essentially uninfluenced by the change in surface conditions after the thermal penetration depth, and it remains at ambient temperature.

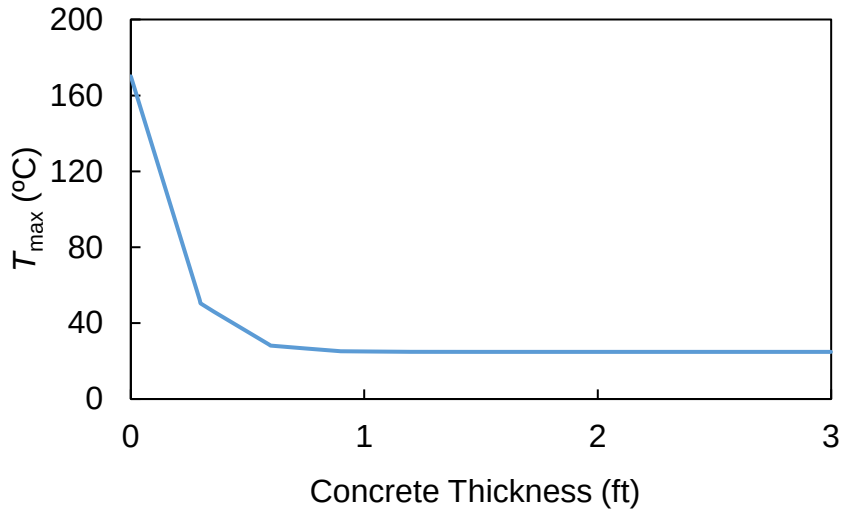

Figure 30: Temperature variation across concrete slab (the location of the surface was chosen at the maximum surface temperature) at *t* = 60 min for the 20 MW hydrocarbon fire inside the CANA tunnel with no ventilation. A thermal penetration depth of δ_p = 7.5 inches (0.19 m) is observed where the concrete temperature linearly decreases from 170°C to 25°C.

4.2.6.3. CANA Tunnel Without Ventilation

4.2.6.3.1. CFD Simulation Results

The heated gas hydrogen/air mixture (100°C to 2,100°C) inside the CANA Tunnel after 3 seconds of the TPRD activation is illustrated in Figure 31. The view is from one side, traffic flows from left to right, and the hydrocarbon vehicle (blue) and the overturned H_2 vehicle are positioned in the middle of the tunnel. The H_2 jet flame is already impinging on the tunnel ceiling, and the heated gas mixture is expanding in all directions on the ceiling surface. It is important to recognize that Figure 31 is not a representation of only the H_2 jet flame, but a representation of the heated gas mixture inside the tunnel.

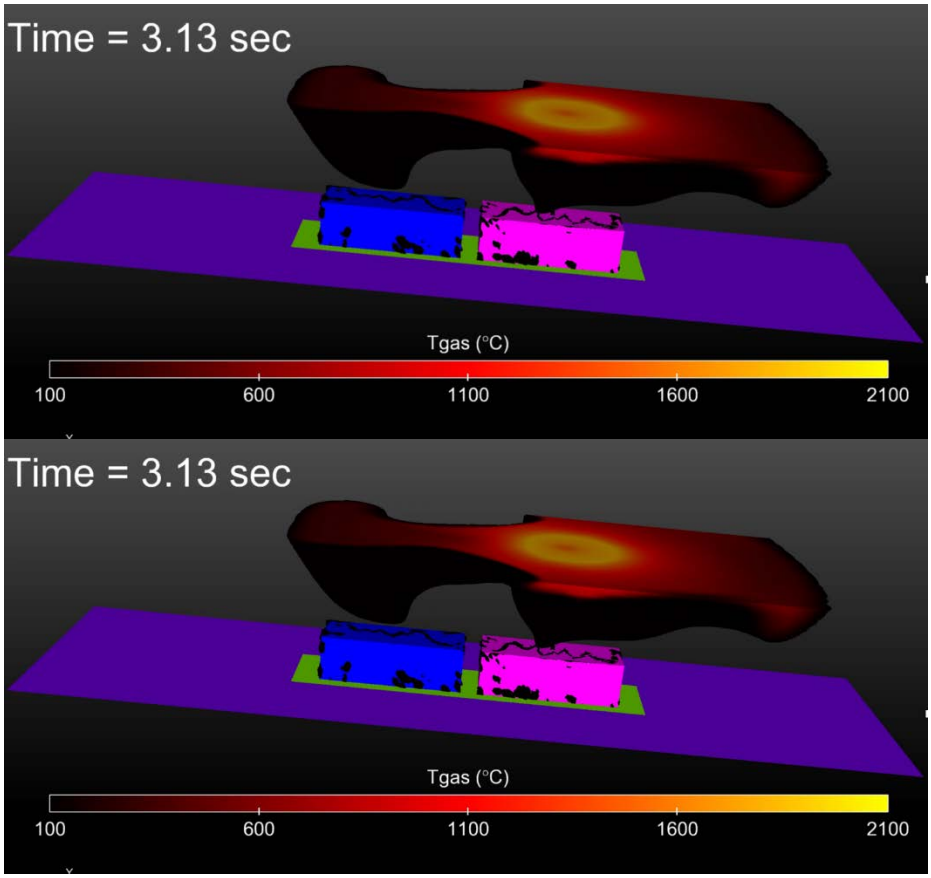

Figure 31: Instantaneous illustration of heated mixture for the H_2 jet CFD simulation of the CANA Tunnel without ventilation.

Figure 32 shows the temperature contours at the location of the H_2 jet flame. At the centerline of the H_2 jet flame close to the orifice, the H_2 flammable mass is higher than 75% at a temperature close to ambient temperature. This means that H_2 does not ignite close to the orifice.

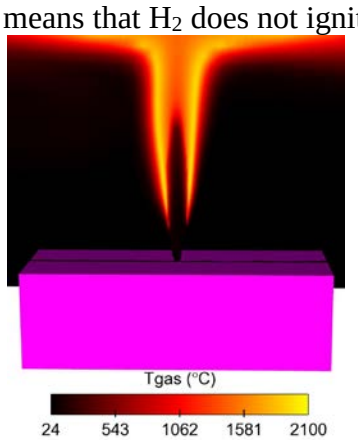

Figure 32: CANA CFD simulation with no ventilation. Cross-sectional view of temperature contours at flame loacation.

The growth of the gas mixture temperature contours at the ceiling interface is shown in Figure 33. The heated gas mixture and flame reach the ceiling in 0.5 seconds, forming circular temperature contours (larger than the ones shown for the H_2 flammable mass). The gas mixture at temperature

higher than 1,000°C reaches a pseudo-steady state at 1 second. A maximum temperature of 1,846°C was reached at the ceiling interface at the contour diameter of 12 feet (3.66 m). The heated gas mixture starts to expand at the ceiling interface until it reaches the side walls of the tunnel at 2 seconds. When the hydrogen is released by the TPRD, the air close to the vehicles gets displaced, and creates a turbulent flow at the bottom of the tunnel. Once it reaches the side walls, the cold air flow starts rising to the ceiling. At 2.2 seconds, the cold air reaches the ceiling and starts mixing with the heated gas mixture creating the disrupted circular shape of the temperature contours shown at t = 3.1 seconds.

The CFD heat transfer coefficient, gas mixture reference temperature, and incident radiation flux were used as boundary conditions on the ceiling structure in the Aria model. The temperature contours shown in Figure 33 are an example of the boundary condition mapped on the surface in the transient Aria model. The CFD simulation was run for only 25 seconds due to computational time limitations. Since no significant change was observed on the heat transfer coefficient, gas mixture reference temperature, and incident radiation flux results after 1 second of the TPRD activation, the solution at 25 seconds was used for the remainder of the H_2 release duration (5 minutes). A maximum heat transfer coefficient of 30 W/m^2-K is achieved in less than one second, and it remains constant for the H_2 release duration. The maximum reference gas mixture temperature observed is 1,846°C. The maximum incident heat flux at the ceiling surface was 174 kW/m^2.

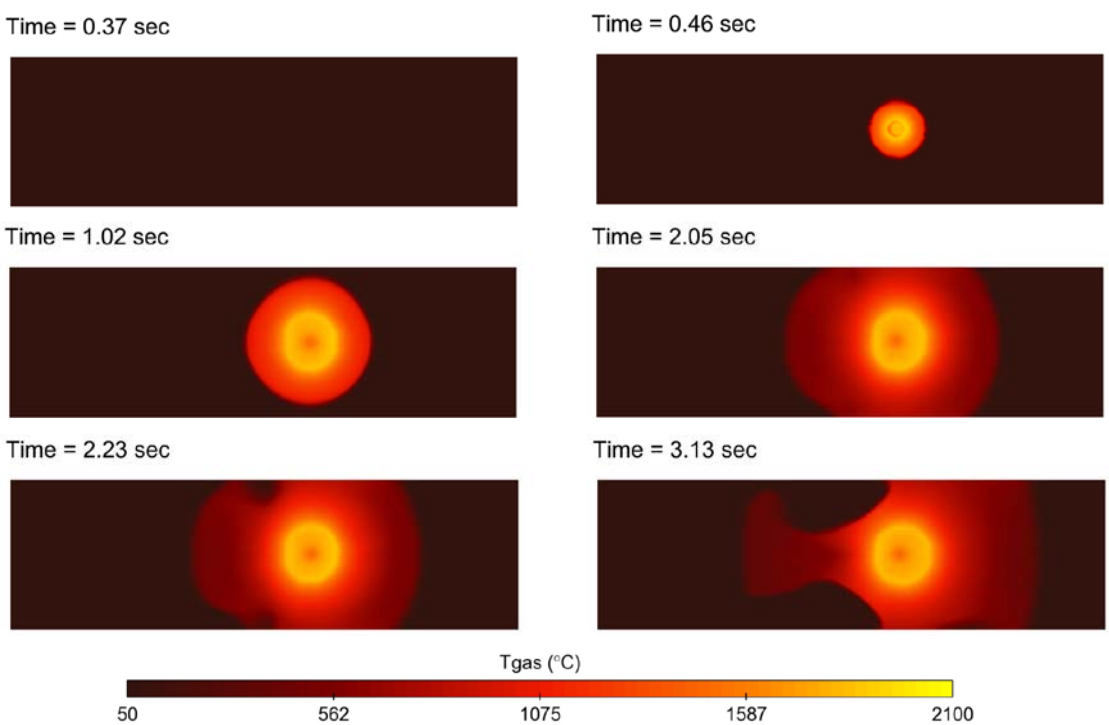

Figure 33: Gas mixture temperature progression at the ceiling interface (t = 0.37–3.13 seconds) for the CANA Tunnel case with no ventilation.

4.2.6.3.2. Heat Transfer Simulation

The temperature variation with position and time of the solid ceiling structure was calculated by applying the boundary conditions described in Section 4.2.6.3.1 Figure 34 shows the surface

temperature of the concrete surface (bottom) in direct contact with the heated gas mixture (top) after the 5 minute H_2 release. The concrete surface temperature is significantly lower than the gas mixture temperature at the ceiling interface.

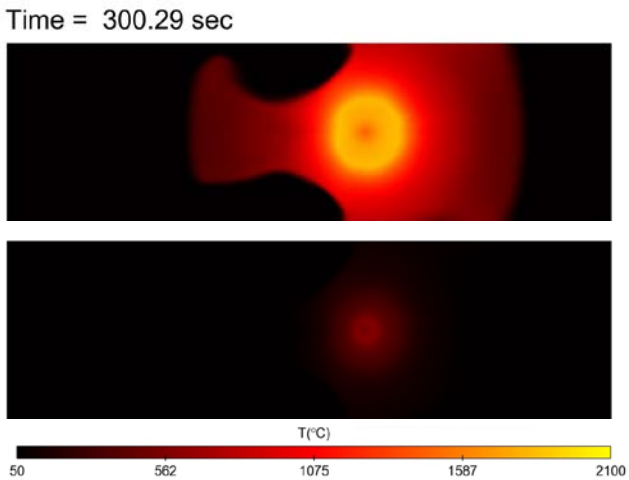

Figure 34: Temperature of the gas mixture (top) and the concrete inner surface (bottom) at *t* = 5 min for the CANA Tunnel with no ventilation.

Figure 35 compares the maximum temperature of the gas mixture and the maximum concrete temperature. The concrete temperature slowly increases with time until it reaches a maximum temperature of 592°C at the end of the H_2 release. The concrete responds slowly to changes in the thermal environment because of its high thermal capacitance (Equation 7). A temperature difference of 1,254°C is observed between the maximum temperature of the gas mixture and the maximum concrete temperature. The duration of the H_2 release is not long enough to raise the concrete temperature closer to the gas temperature significantly.

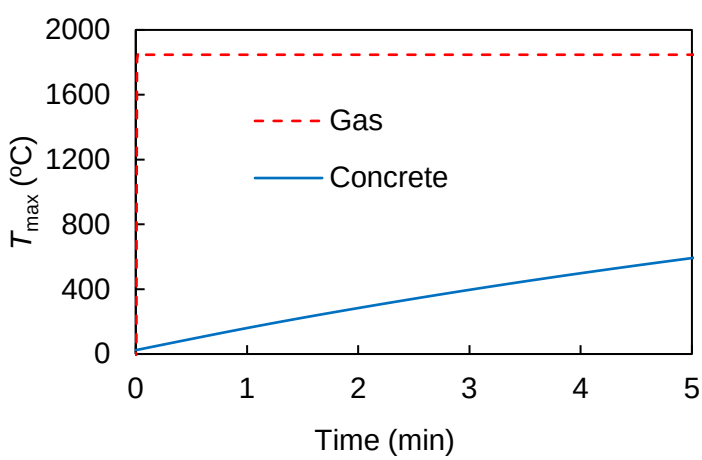

Figure 35: Maximum temperature as a function of time for the CANA Tunnel with no ventilation of the gas mixture (dash-red line) and the concrete (continuous-blue line).

The temperature variation across the concrete thickness was plotted at the location of the maximum surface temperture. A thermal penetration depth of δ_p = 4 inches (0.10 m) is observed where the

concrete temperature linearly decreases from 592°C to 31°C. The concrete slab is essentially uninfluenced by the change in surface conditions after the thermal penetration depth, and it remains at ambient temperature. It is important to mention that in these analyses, the heat release rate from a hydrocarbon fire is not included. If the duration of the hydrocarbon fire is longer than the duration of the H_2 flame, the thermal penetration depth may increase. However, the temperature at the surface would decrease with time.

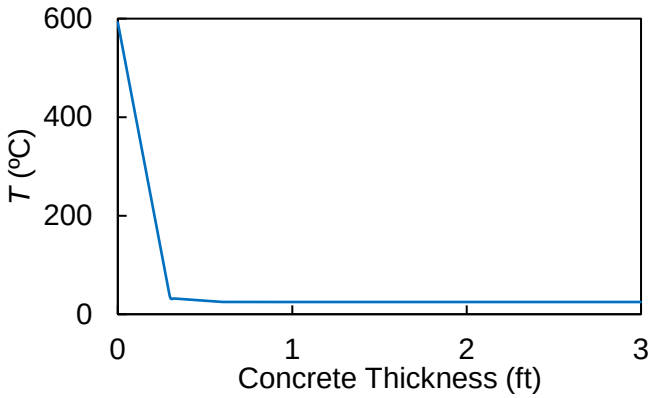

Figure 36: Temperature variation across concrete slab (the location of the surface was chosen at the maximum surface temperature) at *t* = 5 min.

4.2.6.3.3. Solid Mechanics Simulation

In order to determine if the conditions were present for concrete spalling to occur, the maximum surface temperature and the maximum deflection on the concrete structure were compared with the results from Ali et al. [37]. Figure 37 compares the maximum temperature on the CANA concrete ceiling with the temperatures observed for the hydrocarbon fire and ISO 834 experiments. Ali et al observed concrete spalling once the concrete surface temperature reached 750°C, which happened after 2 minutes in the hydrocarbon test and 15 minutes in the ISO834 test. The maximum temperature observed in the CANA tunnel is below the hydrocarbon fire results, which indicates that spalling is not a concern at very early times. At approximately 2.5 minutes, the CANA maximum ceiling surface temperature exceed the temperature observed in the ISO 834 fire. However, spalling is still unlikely to occur because the maximum surface temperature reached after the hydrogen release is 592°C, which is significantly below the spalling temperature of 750°C. Additionally, because the simulation used a constant flow of hydrogen throughout the TPRD release, there is significant conservatism in the duration of the jet flame impingement time on the ceiling. In reality, as the tank pressure decreases during the release, the jet flame will become shorter and shorter until the hydrogen flame burns itself out.

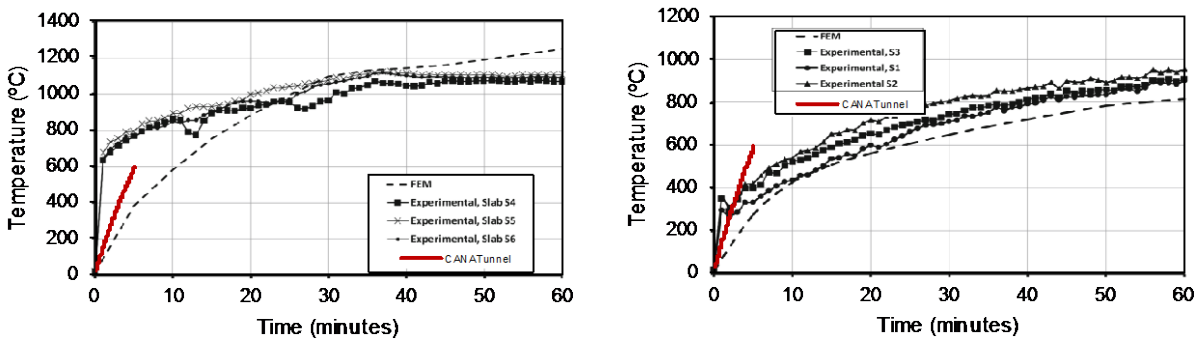

Figure 37: Comparison of maximum surface temperature observed on the CANA concrete ceiling (without ventilation) and the maximum surface temperature observed in the experiments done by Ali et al. [37] under hydrocarbon curve (right) and ISO 834 (left).

It is also important to calculate the deflection of the concrete slab since Ali et al. structure is different from the CANA structure (see Table 4). The temperature distribution of the concrete slab obtained with the Aria model was inputted in the Adagio model to calculate the maximum deflection as a function of time. Figure 38 compares the maximum deflection of the CANA concrete structure and the deflection of the hydrocarbon fire experiment. The deflection of the CANA structure is higher than the deflection of the hydrocarbon fire experiment at 5 minutes. The authors observed concrete spalling after 2 min for the hydrocarbon heating at a surface temperature of approximately 750°C. The temperature and deflection results give contradicting results, so it cannot be ensured that concrete spalling will not happen for this scenario.

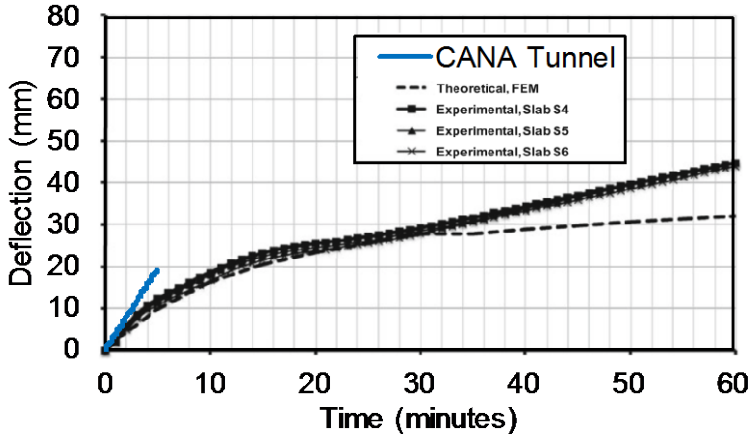

Figure 38: Comparison of maximum deflection observed in the CANA concrete ceiling (without ventilation) and the maximum deflection observed in the experiments done by Ali et al. [37] under hydrocarbon curve.

4.2.6.4. CANA Tunnel with Ventilation

4.2.6.4.1. CFD Simulation

For this scenario, the simulation was run for 75 seconds with no H_2 release in order to achieve a stable laminar air flow from the inlet to the outlet of the tunnel. At 75 seconds, the H_2 release was activated. The extent of the H_2 jet in the air cross-flow can be observed in Figure 39, where the

heated hydrogen/air mixture (100°C to 2,100°C) at t = 5.8 seconds is illustrated. The heated gas mixture reaches the ceiling at a lower temperature than the case with no ventilation. A counter-rotating vortex pair generated by the jet in crossflow caused the separation of the jet at the ceiling interface.

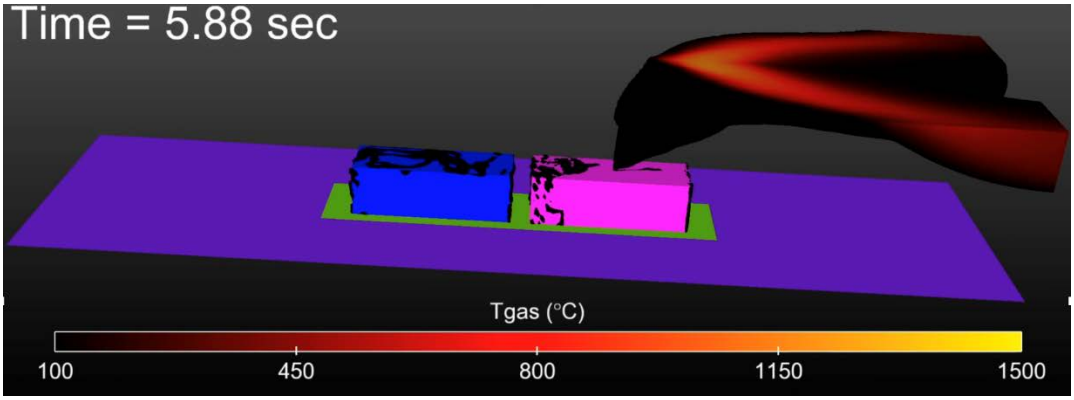

Figure 39: Instantaneous illustration of heated mixture for the H_2 jet CFD simulation with ventilation.

Figure 40 shows the instantaneous temperature contours at the location of the H_2 jet flame. The H_2 does not ignite close to the orifice, resulting in a temperature close to ambient at this location. The jet trajectory close to the jet exit is almost vertical due to the high H_2 jet exit velocity. Once hydrogen enters the tunnel domain, it interacts with the crossflow air as it moves away from the jet exit and begins to bend in the ventilation flow direction. The heated gas mixture does reach the ceiling surface and contributes to the convective heat transfer on the surface. The case with no ventilation will have a higher heat flux on the surface than the case with ventilation.

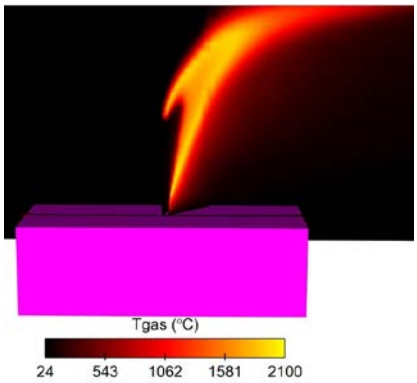

Figure 40: Instantaneous contours of temperature profile for the H_2 jet CFD simulation for the CANA Tunnel with ventilation (t = 5.8 seconds).

The growth of the gas mixture temperature contours at the ceiling interface is shown in Figure 41. The heated gas mixture reaches the ceiling in 1 second, forming elliptical temperature contours. At t = 2 seconds, the effect of the counter-rotating vortex pair created by the jet in crossflow can be observed. The jet starts separating into two streams that approach the side walls as they exit the tunnel are created (t = 3 seconds). The maximum thickness of the heated stream is 7 ft (2.13 m). The CFD heat transfer coefficient, gas mixture reference temperature, and incident radiation flux were used as boundary conditions on the ceiling surface in the Aria model. The gas mixture

reference temperature contours shown in Figure 41 are an example of the boundary condition mapped on the ceiling surface in the transient Aria model. The CFD simulation was run for only 6 seconds due to computational time limitations. Since no significant change was observed on the heat transfer coefficient, gas mixture reference temperature, and incident radiation flux results after 5 seconds, the solution at 6 seconds was used for the rest of the H_2 release duration (5 minutes). A maximum heat transfer coefficient of 20 W/m^2-K is achieved in less than one second, and it remains constant for the H_2 release duration. The maximum reference gas mixture temperature observed is 1,152°C. The maximum incident heat flux at the ceiling surface was 114 kW/m^2.

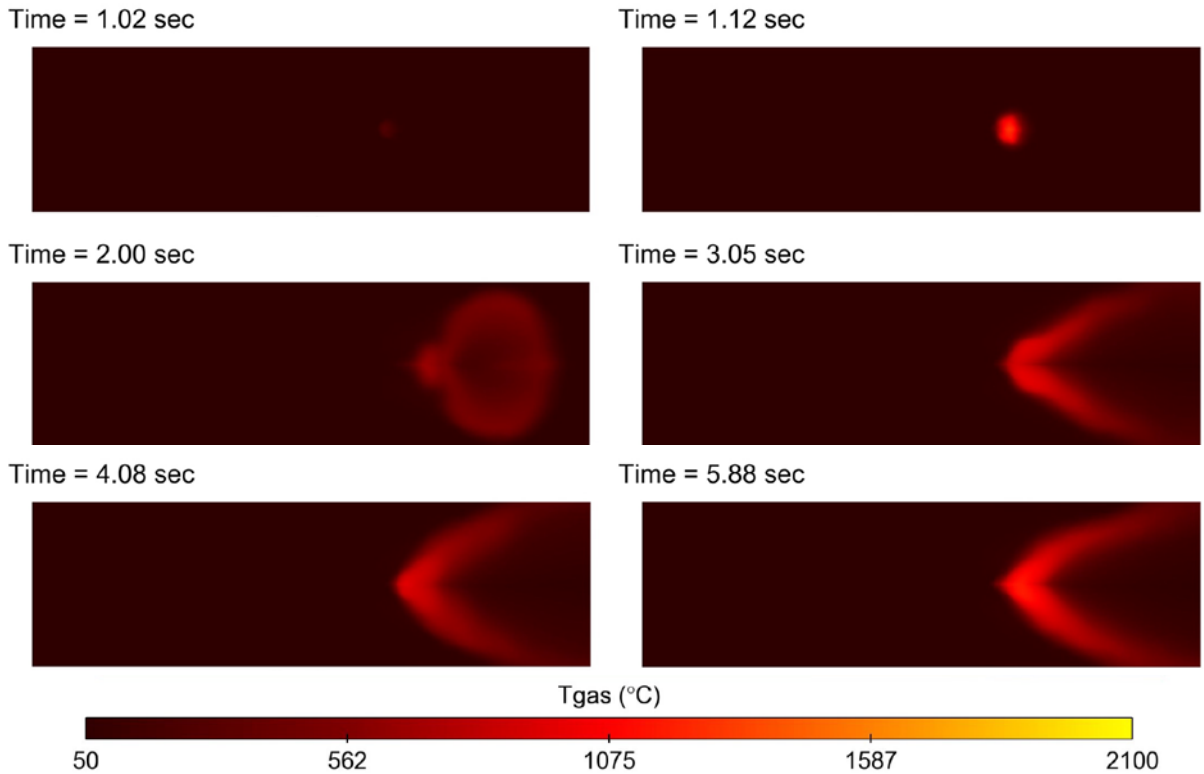

Figure 41: Gas mixture temperature progression at the ceiling interface (t = 1.02–5.88 seconds) for the CANA Tunnel with ventilation.

4.2.6.4.2. Heat Transfer Simulation

The temperature variation with position and time of the solid ceiling structure was calculated by applying the boundary conditions described in Section 4.2.6.4.1. Figure 42 shows the surface temperature of the concrete surface (bottom) in direct contact with the heated gas mixture (top) after the 5 minutes of the H_2 release. The concrete surface temperature is significantly lower than the gas mixture temperature at the ceiling interface.

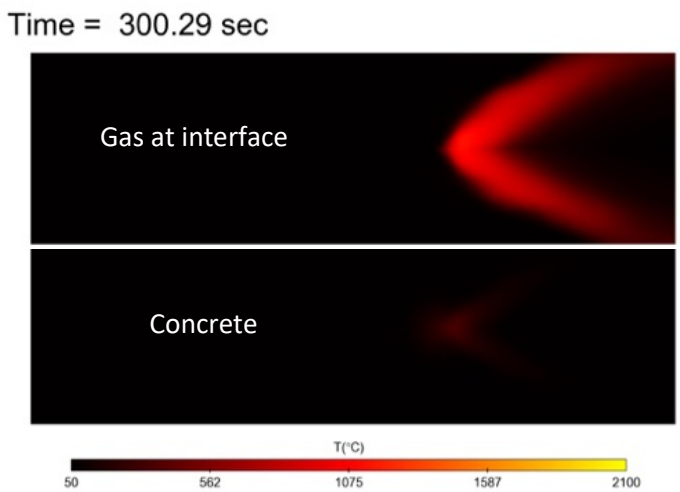

Figure 42: Temperature of the gas mixture (top) and the concrete inner surface (bottom) at *t* = 5 min for the CANA Tunnel with ventilation.

Figure 43 compares the maximum gas mixture temperature and the maximum concrete temperature. The concrete temperature slowly increases with time until it reaches a maximum temperature of 336°C at the end of the H_2 release. A temperature difference of 814°C is observed between the maximum temperature of the gas mixture and the maximum concrete temperature. The duration of the H_2 release is not long enough to raise the concrete temperature closer to the gas temperature. The maximum concrete temperature for the case with ventilation is 256°C lower than the maximum concrete temperature for the case with no ventilation. A ventilation of 10 mph (4.47 m/s) prevents the ceiling temperature to reach temperatures observed in the no ventilation case.

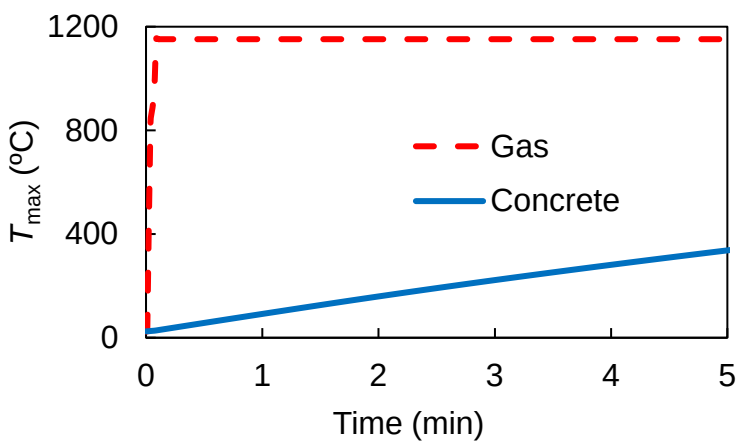

Figure 43: Maximum temperature as a function of time for the CANA Tunnel with ventilation of the gas mixture (dash-red line) and the concrete (continuous-blue line).

The temperature variation across the concrete thickness was plotted at the location of the maximum surface temperture. A thermal penetration depth of δ_p = 4 inches (0.10 m) is observed where the concrete temperature linearly decreases from 336°C to 29°C. The concrete slab is essentially unaffected by the change in surface conditions after the thermal penetration depth, and it remains

at ambient temperature. The thermal penetration depth was the same for both cases, with and without ventialtion since δ_p is only dependent on the solid properties.

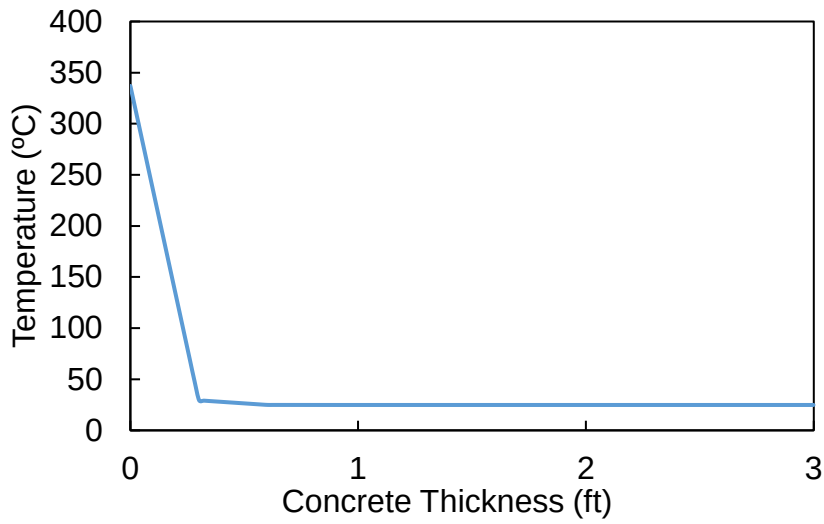

Figure 44: Temperature variation across concrete slab (the location of the surface was chosen at the maximum surface temperature) at *t* = 5 min.

4.2.6.4.3. Solid Mechanics Simulation

In order to determine if the conditions were present for concrete spalling to occur, the maximum surface temperature and the maximum deflection on the concrete structure were compared with the results from Ali et al. [37]. Figure 45 compares the maximum temperature on the CANA concrete ceiling with the temperatures observed for the ISO 834 and hydrocarbon fire experiments. The authors started to observe concrete spalling after 15 minutes for the ISO 834 heating test at temperatures higher than 750°C. The maximum temperature observed in the CANA concrete structure for the ventilation case is lower than the ISO 834 and hydrocarbon fire experiments at all times, which indicates that spalling in this case scenario is not likely to occur.

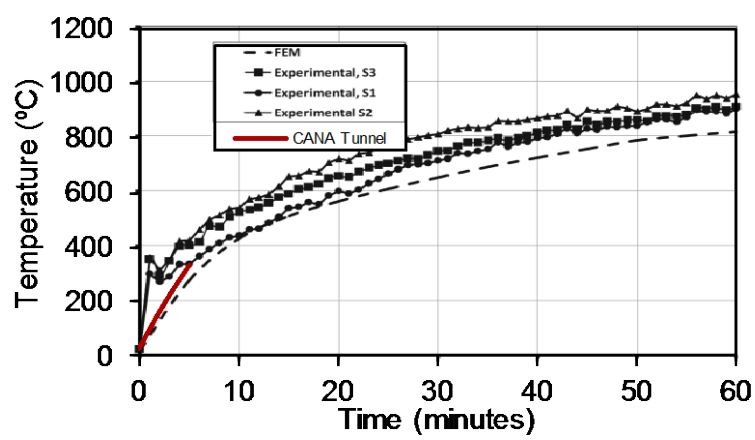

Figure 45: Comparison of maximum temperature observed on the CANA concrete ceiling (with ventilation) and the maximum temperatures observed in the experiments done by Ali et al. [37] under the ISO 834 curve.

Figure 46 compares the maximum deflection of the CANA concrete structure and the deflection of the ISO 834 fire experiment. A maximum deflection of 7.6 mm was observed in the CANA Tunnel, which is higher than the deflection observed in the ISO 834 fire experiment at 5 minutes. Concrete spalling was observed after 15 minutes for the ISO 834 heating at a surface temperature of approximately 750°C. The deflection at 15 minutes was 10 mm, which is higher than the CANA maximum deflection. The temperature and deflection results indicate that concrete spalling is unlikely to happen in this scenario. It is important to reiterate that the hydrogen heat release rate was over-predicted due to conservative assumptions, so the temperature observed will be lower resulting in a lower deflection.

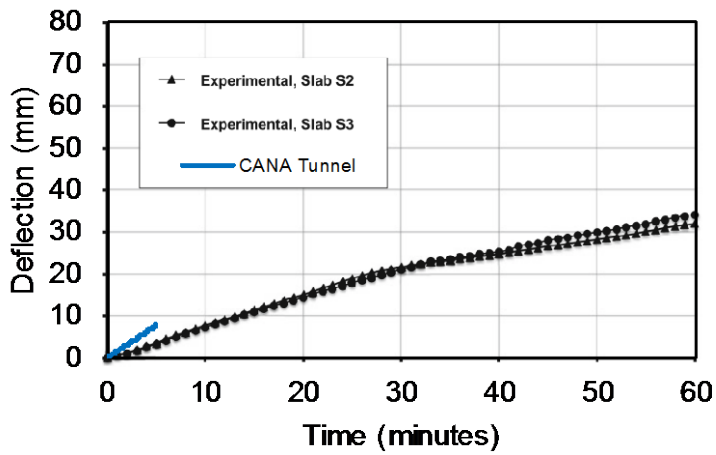

Figure 46: Comparison of maximum deflection observed on the CANA concrete ceiling (with ventilation) and the maximum deflection observed in the experiments done by Ali et al. [37] for the ISO 834 curve.

4.2.6.5. Ted Williams Tunnel Without Ventilation

4.2.6.5.1. Heat Transfer Simulation

The temperature variation with position and time of the solid ceiling structure was calculated by applying the boundary conditions described in Section 4.2.6.3.1. The bottom illustration of Figure 47 shows the surface temperature of the Ted Williams Tunnel ceiling surface (concrete panels and stainless steel hangers) in direct contact with the heated gas mixture (top illustration) after the 5 minutes of the H_2 release. The concrete surface temperature is significantly lower than the gas mixture temperature at the ceiling interface, and the stainless steel surface temperature is significantly lower than the concrete surface temperature.

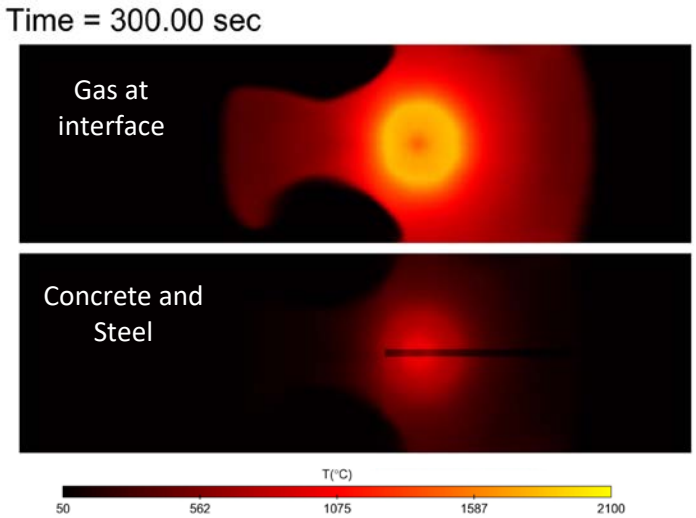

Figure 47: Temperature of the gas mixture (top) at the ceiling interface and temperature of concrete and stainless steel structure(bottom) at *t* = 5 min for the Ted Williams Tunnel with no ventilation.

Figure 48 compares the maximum temperature of gas mixture temperature, the concrete, and the stainless steel hangers. The concrete temperature slowly increases with time until it reaches a maximum temperature of 1,089°C at the end of the H_2 release, while the stainless steel hangers reach a maximum temperature of 706°C. The reason the stainless steel is at a lower temperature is that the thermal diffusivity for stainless steel is larger than the thermal diffusivity of concrete. The same heat flux is being applied to both the stainless steel and the concrete, but heat will conduct faster than in the concrete resulting in a lower temperature in the stainless steel surface. A temperature difference of 782°C is observed between the maximum temperature of the gas mixture and the maximum concrete temperature. The temperature of the surface of the concrete panels in the Ted Williams Tunnel is higher than the temperature of the surface of the CANA Tunnel concrete slabs at 5 minutes due to the difference in the thickness of the concrete structures.

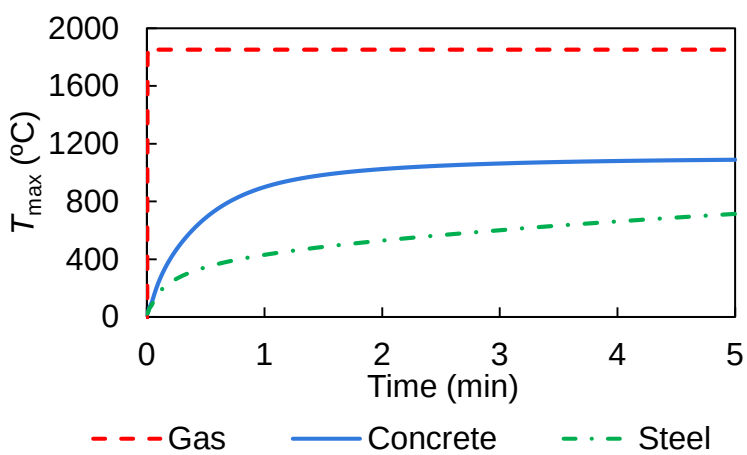

Figure 48: Maximum temperature as a function of time for the Ted Williams Tunnel with no ventilation of: the gas mixture (dash-red line), the concrete (continuous-blue line), and the stainless steel hangers (dash-dot-green line).

The temperature variation along the vertical hanger closest to the flame impingment was plotted in Figure 49. The stainless steel surface in direct contant with the flame was located at L = 0 feet, and the surface attached to the tunnel ceiling bolts anchored to the epoxy was located at L = 1.8 feet (0.55 m). A thermal penetration depth of δ_p = 6 inches (0.15 m) was observed, where the stainless steel temperature decreases from 557°C to ambient temperature. The dash-red line representes the epoxy degradation temperature (90°C) specified by manufacturer. At L = 1.8 feet (0.55 m), the temperature is essentially uninfluenced by the change in surface conditions at L = 0 feet. The expoxy temperature is well bellow the degradation point of 90°C.

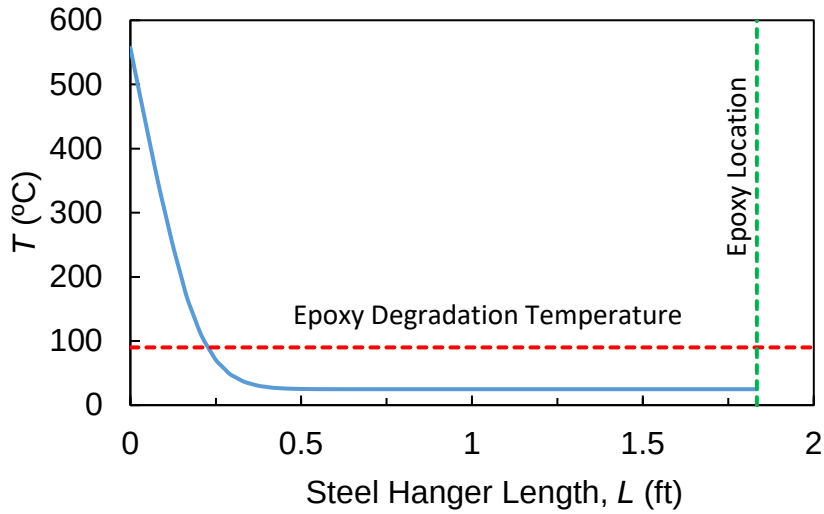

Figure 49: Temperature variation along the vertical hanger closest to the flame impingement for the ventilation case. Dash-red line representes the epoxy degradation temperature, and dash-green line is the location where the hanger is attached to the ceiling with the bolts anchored to the epoxy.

4.2.6.5.2. Solid Mechanics Simulation

4.2.6.5.2.1. Thermal Deflection of Concrete Panels and Stainless Steel Structure

Figure 50 compares the maximum temperature on the Ted Williams Tunnel concrete panels and stainless steel structure with the temperatures observed in the hydrocarbon fire experiments. The maximum temperature observed in the Ted Williams Tunnel concrete panels is significantly higher that than the hydrocarbon fire temperatures, which indicates that spalling in this case scenario is very likely to occur. The Ted Williams concrete panels are thinner than the concrete ceiling in the CANA tunnel, which makes the concrete panels more prone to spalling.

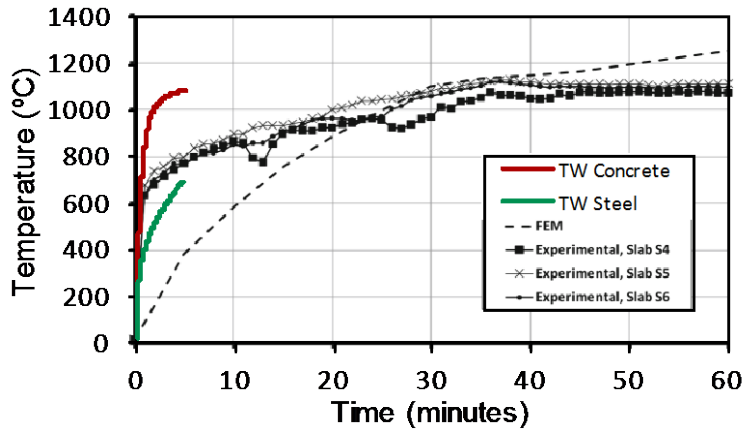

Figure 50: Comparison of maximum temperature observed on the Ted Williams concrete ceiling (without ventilation) and the maximum temperatures observed in the experiments done by Ali et al. [36] under the hydrocarbon curve.

Figure 51 shows the maximum deflection of the Ted Williams concrete panels and stainless steel structure. At 2 minutes, a maximum deflection of 200 mm was observed in the Ted Williams concrete panels, which is significantly higher than the deflection observed in the hydrocarbon fire experiment. The temperature and deflection results indicate that concrete spalling will occur in this scenario. The stainless steel structure had a maximum deflection of 1.3 mm at t = 2 minutes.

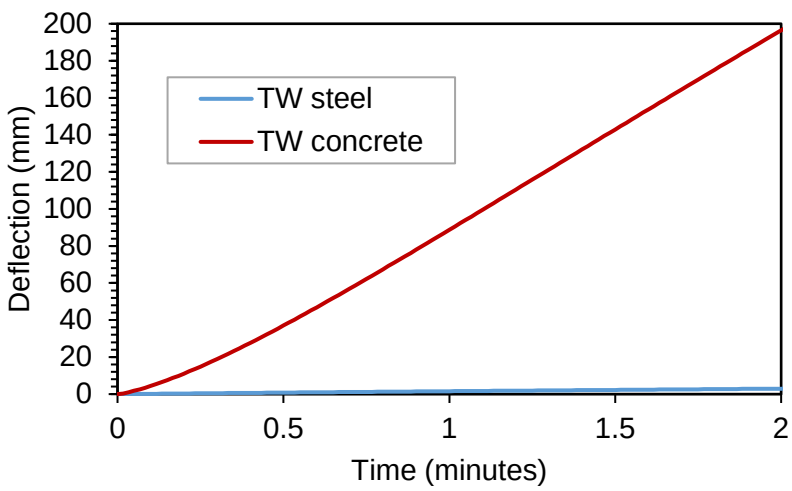

Figure 51: Maximum deflection observed on the Ted Williams Tunnel concrete panels and stainless steel structure (without ventilation).

4.2.6.5.2.2. Yield stress on steel structure

The yield stress at the maximum temperature of the stainless steel structure is 31,148 psi (214.76 MPa), which is significantly higher than the 808 psi (5.57 MPa) total stress on the steel structure due to the weight of the concrete panels. If the structure is ASTM A36 steel, the yield strength is 58,000 psi (399.90 MPa), which is also higher than the 808 psi (5.57 MPa). Therefore, the steel structure will not be compromised.

4.2.6.6. Ted Williams Tunnel with Ventilation

4.2.6.6.1. Heat Transfer Simulation

The temperature variation with position and time of the solid ceiling structure was calculated by applying the boundary conditions described in Section 4.2.6.4.1. The bottom illustration of Figure 52 shows the surface temperature of the Ted Williams Tunnel ceiling surface (concrete panels and stainless steel hangers) in direct contact with the heated gas mixture (top illustration) after the 5 minutes of the H_2 release. The concrete surface temperature is significantly lower than the gas mixture temperature at the ceiling interface, and the stainless steel surface temperature is significantly lower than the concrete surface temperature.

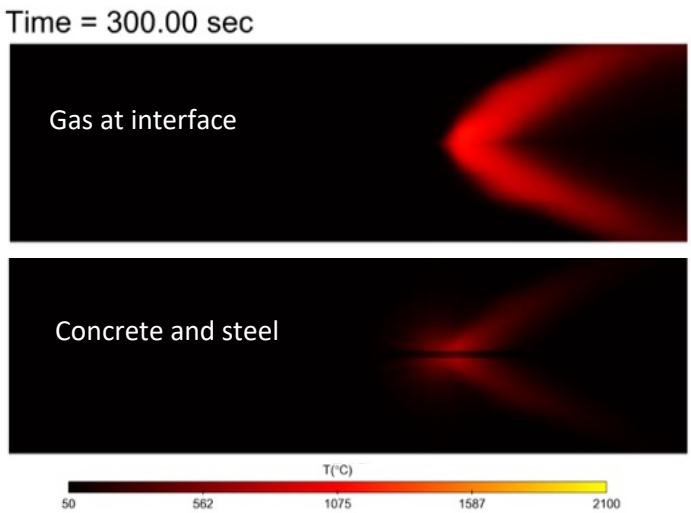

Figure 52: Temperature of the gas mixture (top) at the ceiling interface and temperature of concrete and stainless steel structure(bottom) at *t* = 5 min for the Ted Williams Tunnel with ventilation.

Figure 53 compares the maximum temperature of gas mixture temperature, the concrete, and the stainless steel hangers for the case with ventilation. The maximum gas temperature at the concrete panels interphase is 1151°C. The concrete temperature slowly increases with time until it reaches a maximum temperature of 805°C at the end of the H_2 release, while the stainless steel hangers reach a maximum temperature of 436°C. A temperature difference of 346°C is observed between the maximum temperature of the gas mixture and the maximum concrete temperature. The maximum concrete temperature for the case with ventilation is 283°C lower than the maximum concrete temperature for the case with no ventilation. The maximum stainless steel temperature for the case with ventilation is 270°C lower than the maximum concrete temperature for the case with no ventilation. A ventilation of 10 mph (4.47 m/s) prevents the ceiling temperature from reaching temperatures observed in the case of no ventilation.

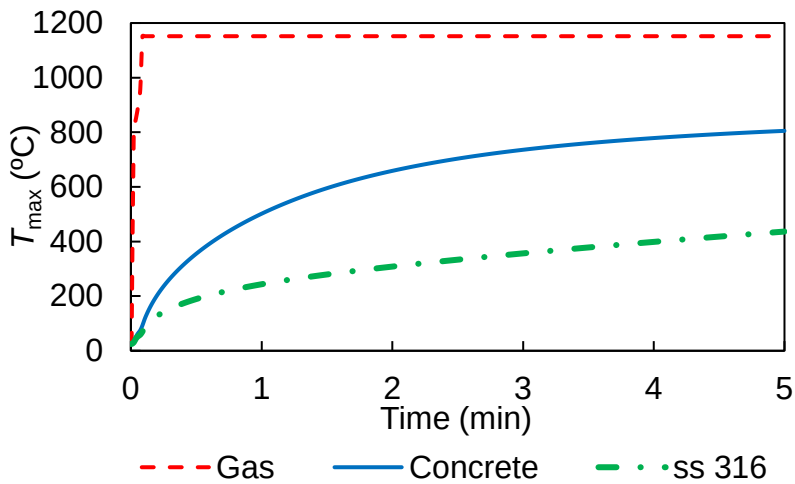

Figure 53: Maximum temperature as a function of time for the Ted Williams Tunnel with ventilation of: gas mixture (dash-red line), the concrete (continuous-blue line), and the stainless steel hangers (dash-dot-green line).

The temperature variation along the vertical hanger closest to the flame impingement was plotted in Figure 54. The stainless steel surface in direct contant with the flame was located at L = 0 feet, and the surface attached to the tunnel ceiling bolts anchored to the epoxy was located at L = 1.8 feet (0.55 m). A thermal penetration depth of δ_p = 6 inches (0.15 m) was observed, where the stainless steel temperature decreases from 344°C to ambient temperature. The dash-red line representes the epoxy degradation temperature (90°C) specified by manufacturer. At L = 1.8 feet (0.55 m), the temperature is essentially uninfluenced by the change in surface conditions at L = 0 feet. The epoxy temperature is well bellow the degradation point of 90°C.

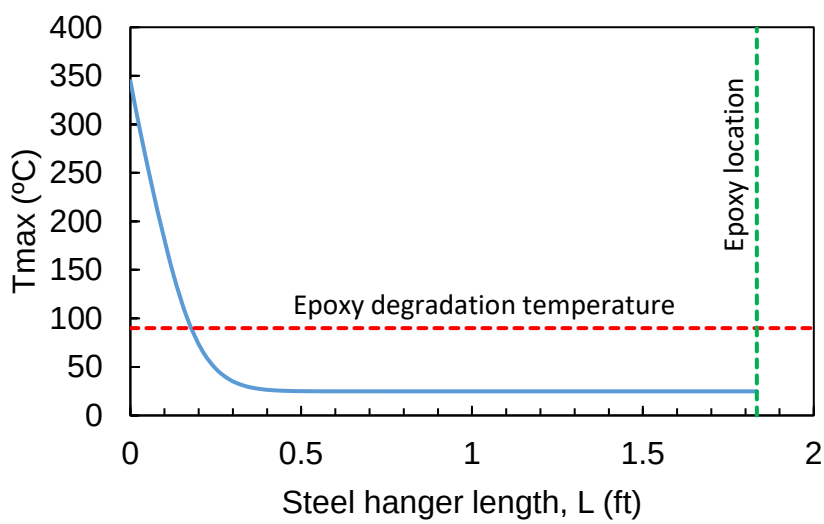

Figure 54: Temperature variation along the vertical hanger closest to the heated gas mixture impingement for the ventilation case. Dash-red line representes the epoxy degradation temperature, and dash-green line is the location where the hanger is attached to the ceiling with the bolts anchored to the epoxy.

4.2.6.6.2. Solid Mechanics Simulation

4.2.6.6.2.1. Thermal Deflection of Concrete Panels and Stainless Steel Structure

Figure 55 compares the maximum temperature on the Ted Williams concrete panels and stainless steel structure with the temperatures observed for the ISO 834 and hydrocarbon fire experiments. The maximum temperature observed in the Ted Williams concrete panels is aligned with the temperature observed in the hydrocarbon fire test, which indicates that spalling in this case scenario may occur. It is important to reiterate that the hydrogen heat release rate was over-predicted, so the actual temperature observed should be lower than that which causes spalling.

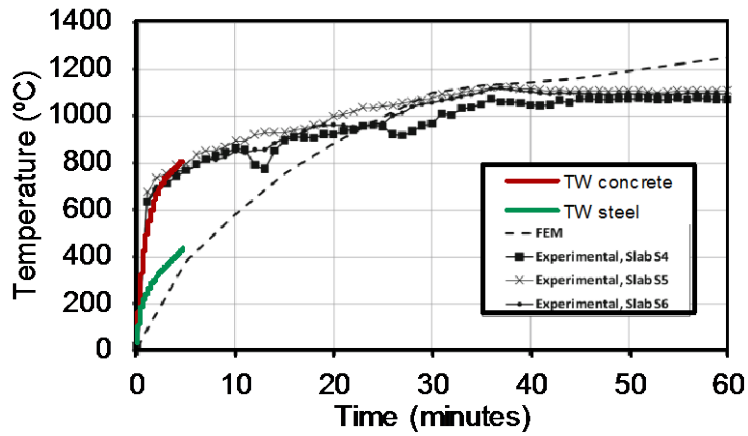

Figure 55: Comparison of maximum temperature observed on the Ted Williams concrete ceiling (with ventilation) and the maximum temperatures observed in the experiments done by Ali et al. [36] under the hydrocarbon curve.

Figure 56 compares the maximum deflection of the Ted Williams concrete panels and stainless steel structure with the deflection of the hydrocarbon fire experiment. A maximum deflection of 43.5 mm was observed in the Ted Williams concrete panels, which is higher than the deflection observed in the hydrocarbon fire experiment at 5 minutes. The temperature and deflection results indicate that concrete spalling is likely to occur in this scenario. The stainless steel structure had a maximum deflection of 1.3 mm at t = 5 minutes.

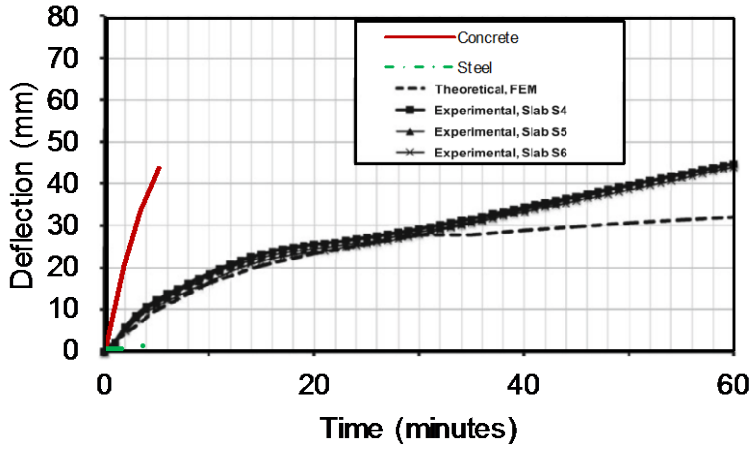

Figure 56: Comparison of maximum deflection observed on the Ted Williams concrete panels and stainless steel structure (with ventilation) and the maximum concrete deflection observed in the experiments done by Ali et al. [36].

4.2.6.6.2.2. Yield stress on steel structure

The yield stress at the maximum temperature of the stainless steel structure is 21,435 psi (147.79 MPa), which is significantly higher than the 808 psi (5.57 MPa) total stress on the steel structure due to the weight of the concrete panels. If the structure is ASTM A36 steel, the yield strength is 25,000 psi (172.37 MPa), which is also higher than the 808 psi (5.57 MPa). Therefore, the steel structure will not be compromised.

5. SUMMARY AND CONCLUSIONS

To provide a comprehensive analysis of the potential risks and hazards related to FCEV incidents in tunnels, a risk analysis was performed to estimate what scenarios were most likely to occur in the event of a crash. Some factors lack specific and directly applicable data, but the most likely consequence of a crash is no additional hazard from the hydrogen. This includes minor crashes, and a variety of scenarios in which the hydrogen is not released or does not ignite. Of the scenarios in which hydrogen does ignite, by far the most likely is a jet flame resulting from the release of hydrogen through the TPRD due to the heat from a typical accident-related hydrocarbon fire. This scenario was considered further in detailed modeling of specific tunnel configurations and scenarios to better illustrate the potential effects of this type of hazard.

Throughout the modeling and simulation, several assumptions had to made, either because the precise information was not available or to allow the simulation to run in a time-efficient manner. The CFD model in particular required one to weeks hours to run on SNL's extensive computing facilities. The assumptions were documented throughout this report, and in all cases, the most conservative assumption was made to ensure the worst cases consequence was analyzed. The impacts and magnitude of the conservatism cannot always be quantified, however in the case of the mass flow rate of the hydrogen jet flame, the increased total mass of hydrogen released can be calculated. The total mass contained in a typical FCEV tank is 5 kg of hydrogen. In the CFD simulation, the size of the orifice of the TPRD was 5 cm instead of the 2 mm typical orifice and the release was modeled at the maximum flow rate for the entire 5-minute release duration. This resulted in a total release of 29 kg of hydrogen in the model. The six-fold overestimate of hydrogen release certainly resulted in an increase of the total heat released by the jet flame as well as the constant full height of the flame. These factors influence the potential for spalling of the concrete surfaces.

A summary of the maximum temperature and deflection for the CANA and Ted Williams structures is presented in Table 6. The worst-case scenarios were seen when the ventilation is not operating. Both the CANA and Ted Williams Tunnel results show that the thermal conditions may result in localized spalling in the area where the hydrogen jet flame impinges the ceiling. If the ventilation is operating, the maximum temperature is significantly lower, and spalling is not expected to occur. The total stress on the steel structure was significantly lower than the yield stress of stainless steel and ASTM A36 at the maximum steel temperature even when the ventilation was not on. Therefore, the steel structure will not be compromised. The temperature of the epoxy remains at ambient temperature, which is well below the degradation point of 90ºC. This is true for both scenarios: with and without ventilation. The maximum temperature of the stainless steel hanger exposed directly to the hydrogen jet flame is 706ºC after 5 minutes of impingement for the case with no ventilation, which results in a maximum deflection of 7 mm. This result for the deflection due to the thermal expansion will not impact the structural integrity of the beam. It is important to reiterate that the hydrogen heat release rate was over-predicted, so the temperature observed should be lower than that which results in spalling.

Table 6: Summary of the maximum surface temperature and deflection for the CANA and Ted Williams Tunnel structures.

Fire Curve		Maximum Temperature (ºC)	Maximum Deflection (mm)	Yield Stress (MPa)
Hydrocarbon		~750	~5	-
ISO 834		~750	~10	-
H_2 Jet Flame CANA (NV)		592	19.4	-
H_2 Jet Flame CANA (V)		336	7.6	-
H_2 Jet Flame TW (NV)	Concrete	1,088	< 200	-
	Stainless Steel	706	~7	147.79
	ASTM A36	-	-	399.90
H_2 Jet Flame TW (V)	Concrete	805	43.5	-
	Stainless Steel	436	1.3	214.76
	ASTM A36	-	-	172.37

The results of this analysis and modeling effort will assist the local authorities that have jurisdiction over road tunnels in evaluating the requirements for FCEVs in tunnels.

APPENDIX A

A.1. Previous Alternate Fuel Vehicle Studies

In 1994-1995, a hazard analysis was completed by Worchester Polytechnic Institute (WPI) on the alternate fuel vehicles in tunnels and included CNG, liquefied petroleum gas (LPG), and liquefied natural gas (LNG) (hydrogen was not included) [59]. These studies were performed for the large tunnel construction projects happening at that time in Boston (Ted Williams Tunnel). These studies specifically excluded both the extremely small release scenarios (resulting in a loose fitting in the fuel system and a slow small leak) as well as the tank rupture scenario. The basis for excluding the tank rupture scenario was that the CNG tank industry standards include specific regulations on the fuel system integrity and the required tank testing which ensure resilient tanks. The venting of CNG due to an external fire scenario was also eliminated because the external fire presented an existing hazard and an additional jet fire of CNG was deemed to be not significant enough to drive the evaluation. Additionally, if the venting CNG did not immediately ignite, it was assessed that the fire induced buoyancy would enhance the dispersion of the released gas.

The basis of the 1994-1995 CNG tunnel safety evaluation was made by a detailed analysis of the fuel line break scenario for two CNG vehicles: a large passenger van and a school bus. These CNG fuel line releases were compared to analogous gasoline fuel line breaks and the subsequent vaporization of the gasoline pool. The results of this study determined that the size and duration of flammable vapor regions are highly dependent on the tunnel ventilation rates. For all ventilation rates examined, the expected size and duration of a flammable vapor cloud was less than the equivalent gasoline scenario. Also, the flammable cloud of natural gas would not persist for more than a few minutes before dissipating. The fire consequence analysis concluded that the gasoline spill would result in a larger heat release rate and larger smoke cloud than the CNG fire. As a result of this study, a policy allowing CNG vehicles in Massachusetts tunnels was adopted.

REFERENCES

[1] F. A. Rigas, Paul, *Hydrogen Safety*. Boca Raton: CRC Press, 2013.

[2] National Fire Protection Association, *NFPA 502, Standard for road tunnels, bridges, and other limited access highways*. NFPA, 2010.

[3] A. Haack, "Technical Report-Part 1-Design Fire Scenarios," *Thematic network on fires in tunnels (FIT), European Commission under the 5th Framework Program*, vol. 2004, 2001.

[4] *Operational & Safety Requirements*.

[5] A. Lönnermark and H. Ingason, "Gas temperatures in heavy goods vehicle fires in tunnels," *Fire safety journal*, vol. 40, no. 6, pp. 506-527, 2005.

[6] D. Van Heerden, "The use of Calcium Aluminate Cement in shotcrete," in *Shotcrete: More Engineering Developments: Proceedings of the Second International Conference on Engineering Developments in Shotcrete, October 2004, Cairns, Queensland, Australia.*, 2004, p. 267: Taylor & Francis.

[7] *Standard Test Methods for Fire Tests of Building Construction and Materials*, 2016.

[8] *Standard for Rapid Rise Fire Tests of Protection Materials for Structural Steel*, 2017.

[9] J. Brekelmans, R. ven den Bosch, and K. Both, "Summary of large scale fire tests in the Runehamar tunnel in Norway," *Published by: UPTUN, TNO, PROMAT*, 2003.

[10] V. Babrauskas and R. D. Peacock, "Heat release rate: the single most important variable in fire hazard," *Fire safety journal*, vol. 18, no. 3, pp. 255-272, 1992.

[11] J. Hall and J. Watts, "Fire risk analysis," *NFPA*, pp. 3-135, 2008.

[12] S. Bassan, "Overview of traffic safety aspects and design in road tunnels," *IATSS Research*, vol. 40, no. 1, pp. 35-46, 2016/07/01/ 2016.

[13] F. H. Amundsen, P. Melvær, and G. Ranes, "Studies on Norwegian road tunnels: an analysis on traffic accidents and car fires in road tunnels, 1997," 1997.

[14] National Highway Traffic Safety Administration (NHTSA), "Traffic Safety Facts 2015: A Compilation of Motor Vehicle Crash Data from theFatality Analysis Reporting System and the General Estimates System," National Center for Statistics and Analysis, U.S. Department of Transportation, Washington, DC, DOT HS 812384, 2015.

[15] D. Pape and A. Cox, "Compressed Hydrogen Container Fueling Options for Crash Testing," National Highway Traffic Safety Administration, Washington, DC, DOT HS 812 133, May, 2015 2015.

[16] B. M. Institute, "Crashworthiness Research of Prototype Hydrogen Fuel Cell Vehicles: Task Order 7 Project Report," National Highway Traffic Safety Administration, Washington, DC, 2015.

[17] D. Kelly and C. Smith, *Bayesian inference for probabilistic risk assessment: A practitioner's guidebook*. Springer Science & Business Media, 2011.

[18] A. Tchouvelev, D. Hay, and P. Bénard, "Quantitative risk comparison of hydrogen and CNG refuelling options," Final Technical Report to Natural Resources Canada, 2006.

[19] A. W. Cox, F. P. Lees, and M. L. Ang, *Classification of hazardous locations*. IChemE, 1990.

[20] J. LaChance, W. Houf, B. Middleton, and L. Fluer, "Analyses to support development of risk-informed separation distances for hydrogen codes and standards," *Sandia Report SAND2009-0874*, 2009.

[21] K. M. Groth, J. L. LaChance, and A. P. Harris, "Early-stage quantitative risk assessment to support development of codes and standard requirements for indoor fueling of hydrogen vehicles," *SAND2012-10150, Sandia National Laboratories, Albuquerque, NM,* 2012.

[22] A. Lecocq, M. Bertana, B. Truchot, and G. Marlair, "Comparison of the fire consequences of an electric vehicle and an internal combustion engine vehicle," in *2. International Conference on Fires In Vehicles-FIVE 2012*, 2012, pp. 183-194: SP Technical Research Institute of Sweden. Boras.

[23] K. M. Groth, E. S. Hecht, J. T. Reynolds, M. L. Blaylock, and E. E. Carrier, "Methodology for assessing the safety of hydrogen systems: HyRAM 1.0 technical reference manual," *SAND2015-10216 Sandia National Laboratories, Albuquerque, NM (November 2015),* 2015.

[24] R. L. Alpert, "Calculation of response time of ceiling-mounted fire detectors," *Fire technology,* vol. 8, no. 3, pp. 181-195, 1972.

[25] H. Ingason and A. Lönnermark, "Recent achievements regarding measuring of time-heat and time-temperature development in tunnels," in *1st International Symposium on Safe & Reliable Tunnels, Prague, Czech Republic*, 2004, pp. 4-6.

[26] Personal Communication with Massachusetts Department of Transportation, ed, 2016.

[27] N. T. S. Board, "Highway accident report ceiling collapse in the Interstate 90 connector tunnel Boston, Massachusetts July 10, 2006," *Report. Washington: National Transportation Safety Board,* 2007.

[28] A. ACI, "216.1 M-07: Standard Method for Determining Fire Resistance of Concrete and Masonry Construction Assemblies," *Detroit, USA: American Concrete Institute,* 2007.

[29] E. Committee, "Eurocode2: Design of concrete structures-Part 1-2: General rules-Structural fire design," ENV 1992-1-2, 1995.

[30] M. Hedayati, M. Sofi, P. Mendis, and T. Ngo, "A Comprehensive Review of Spalling and Fire Performance of Concrete Members," *Electronic Journal of Structural Engineering,* vol. 15, p. 1, 2015.

[31] K. D. Hertz, "Limits of spalling of fire-exposed concrete," *Fire safety journal,* vol. 38, no. 2, pp. 103-116, 2003.

[32] K. D. Hertz and L. S. Sørensen, "Test method for spalling of fire exposed concrete," *Fire Safety Journal,* vol. 40, no. 5, pp. 466-476, 2005.

[33] J.-C. Mindeguia, P. Pimienta, H. Carré, and C. L. Borderie, "Experimental analysis of concrete spalling due to fire exposure," *European Journal of Environmental and Civil Engineering,* vol. 17, no. 6, pp. 453-466, 2013.

[34] B. Schrefler, P. Brunello, D. Gawin, C. Majorana, and F. Pesavento, "Concrete at high temperature with application to tunnel fire," *Computational Mechanics,* vol. 29, no. 1, pp. 43-51, 2002.

[35] J. Zhao, J.-j. Zheng, G.-f. Peng, and K. van Breugel, "A meso-level investigation into the explosive spalling mechanism of high-performance concrete under fire exposure," *Cement and Concrete Research,* vol. 65, pp. 64-75, 2014.

[36] V. Kodur, "Spalling in high strength concrete exposed to fire: concerns, causes, critical parameters and cures," in *Advanced Technology in Structural Engineering*, 2000, pp. 1-9.

[37] F. Ali, A. Nadjai, and A. Abu-Tair, "Explosive spalling of normal strength concrete slabs subjected to severe fire," *Materials and structures,* vol. 44, no. 5, pp. 943-956, 2011.

[38] S. S. I. o. N. A. (SSINA). High Temperature Properties [Online]. Available: http://www.ssina.com/composition/temperature.htm
[39] A. B. Williams, "SIERRA Framework Version 4: Solver Services," Sandia National Laboratories, SAND2004-6428, February 2005.
[40] C. D. Moen, G. H. Evans, S. P. Domino, and S. P. Burns, "A Multi-Mechanics Approach to Computational Heat Transfer," in *ASME 2002 International Mechanical Engineering Congress and Exposition*, New Orleans, LA, USA, 2002, pp. 25-32: American Society of Mechanical Engineers.
[41] P. K. Notz, S. R. Subia, M. M. Hopkins, H. K. Moffat, D. R. Noble, and T. O. Okusanya, "SIERRA Multimechanics Module: Aria User Manual – Version 4.40," Sandia National Laboratories, SAND2016-4159, May 2016.
[42] J. A. Mitchell, A. S. Gullerud, W. M. Scherzinger, R. Koteras, and V. L. Porter, "Adagio: non-linear quasi-static structural response using the SIERRA framework," Sandia National Laboratories, SAND2001-1603A, 2001.
[43] SIERRA Solid Mechanics Team, "Sierra/SolidMechanics 4.22 User's Guide," Sandia National Laboratories, SAND2011-7597, October 2011.
[44] J. H. Ferziger and M. Peric, *Computational methods for fluid dynamics*. Springer Science & Business Media, 2012.
[45] T. J. Barth and D. C. Jespersen, "The design and application of upwind schemes on unstructured meshes," 1989.
[46] D. Goodwin, H. K. Moffat, and R. L. Speth, "Cantera: An object-oriented software toolkit for chemical kinetics, thermodynamics, and transport processes," *Caltech, Pasadena, CA*, 2009.
[47] B. Magnussen, B. Hjertager, J. Olsen, and D. Bhaduri, "Effects of turbulent structure and local concentrations on soot formation and combustion in C2H2 diffusion flames," in *Symposium (International) on Combustion*, 1979, vol. 17, no. 1, pp. 1383-1393: Elsevier.
[48] S. Domino, "SIERRA/Fuego/Syrinx Low Mach Fluids/Radiation Transport Code," Sandia National Laboratories, 2007.
[49] S. Burns, "SYRINX–user's manual," *unpublished Sandia National Laboratories Report*, 1999.
[50] S. R. Turns and F. H. Myhr, "Oxides of nitrogen emissions from turbulent jet flames: Part I—Fuel effects and flame radiation," *Combustion and Flame*, vol. 87, no. 3-4, pp. 319-335, 1991.
[51] J. Mangs and O. Keski-Rahkonen, "Characterization of the fire behaviour of a burning passenger car. Part I: Car fire experiments," *Fire Safety Journal*, vol. 23, no. 1, pp. 17-35, 1994.
[52] J. Mangs and O. Keski-Rahkonen, "Characterization of the fire behaviour of a burning passenger car. Part II: parametrization of measured rate of heat release curves," *Fire Safety Journal*, vol. 23, no. 1, pp. 37-49, 1994.
[53] R. Bozinoski, "MassTran Documentation: Release 0.9.0," May 22, 2017 2017.
[54] R. Schefer, G. Evans, J. Zhang, A. Ruggles, and R. Greif, "Ignitability limits for combustion of unintended hydrogen releases: experimental and theoretical results," *international journal of hydrogen energy*, vol. 36, no. 3, pp. 2426-2435, 2011.
[55] W. G. Houf, G. Evans, and R. Schefer, "Analysis of jet flames and unignited jets from unintended releases of hydrogen," *International Journal of Hydrogen Energy*, vol. 34, no. 14, pp. 5961-5969, 2009.

[56] W. G. Houf, G. Evans, I. Ekoto, E. Merilo, and M. Groethe, "Hydrogen fuel-cell forklift vehicle releases in enclosed spaces," *International Journal of Hydrogen Energy*, vol. 38, no. 19, pp. 8179-8189, 2013.
[57] V. Kodur and M. Sultan, "Thermal properties of high strength concrete at elevated temperatures," *ACI SPECIAL PUBLICATIONS*, vol. 179, pp. 467-480, 1998.
[58] V. Kodur, "Properties of concrete at elevated temperatures," *ISRN Civil engineering*, vol. 2014, 2014.
[59] "Hazard Analysis of Alternative Fueled vehicles in CA/T Tunnels, Part 1: CNG Fueled Vehicles," April, 1994 1994.

DISTRIBUTION

1 Nick Barilo
Pacific Northwest National Laboratory
P. O. Box 999
Richland, WA 99352

1 Laura Hill
Office of Energy Efficiency and Renewable Energy EE-3F
U.S. Department of Energy
1000 Independence Ave. S.W.
Washington, DC 20585-1615

1 C. Will James
Office of Energy Efficiency and Renewable Energy EE-3F
U.S. Department of Energy
1000 Independence Ave. S.W.
Washington, DC 20585-1615

1 Jay Keller
Zero Carbon Energy Solutions, Inc.
3534 Brunell Dr.
Oakland, CA 94602

1 Charles Myers
Massachusetts Hydrogen Coalition, Inc.
P.O. Box 57
Medway, MA 02053

1 Joseph Rigney
Massachusetts Department of Transportation
10 Park Plaza, Suite 4160
Boston, MA 02116

1 Carl Rivkin
National Renewable Energy Laboratory
15013 Denver West Parkway
Golden, CO 80401

1	MS0748	Brian D. Ehrhart	8851
1	MS0748	Chris B. LaFleur	8851
1	MS0748	Alice B. Muna	8851
1	MS9957	Myra Blaylock	8253
1	MS9957	Gabriela Bran-Anleu	8253
1	MS9957	William G. Houf	8253
1	MS9161	Jonathan A. Zimmerman	8367
1	MS0899	Technical Library	9536 (electronic copy)

Sandia National Laboratories